

# Dynamic Emission Baffle Inspired by Horseshoe Bat Noseleaves

Yanqing Fu

Dissertation submitted to the Faculty of the  
Virginia Polytechnic Institute and State University  
in partial fulfillment of the requirements for the degree of

Doctor of Philosophy  
in  
Engineering Mechanics

Rolf Müller, Chair  
Alexander Leonessa  
Hongxiao Zhu  
Nicole Abaid  
Sunny Jung

January 29, 2016  
Blacksburg, Virginia

Keywords: Noseleaf, Biosonar, Emission Baffle  
Copyright 2016, Yanqing Fu

# Dynamic Emission Baffle Inspired by Horseshoe Bat Noseleaves

Yanqing Fu

(ABSTRACT)

The evolution of bats is characterized by a combination of two key innovations - powered flight and biosonar - that are unique among mammals. Bats still outperform engineered systems in both capabilities by a large margin. Bat biosonar stands out for its ability to encode and extract sensory information using various mechanisms such as adaptive beamwidth control, dynamic sound emission and reception, as well as cognitive processes. Due to the highly integrated and sophisticated design of their active sonar system, bats can survive in complex and dense environments using just a few simple smart acoustic elements. On the sound emission side, significant features that distinguish bats from the current man-made sonar system are the time-variant shapes of the noseleaves. Noseleaves are baffles that surround the nostrils in bats with nasal pulse emission such as horseshoe bats and can undergo non-rigid deformations large enough to affect their acoustic properties significantly. Behavioral studies have shown that these movements are not random byproducts, but are due to specific muscular action. To understand the underlying physical and engineering principles of the dynamic sensing in horseshoe bats, two experimental prototypes ,i.e. intact noseleaf and simplified noseleaf, have been used. We have integrated techniques of data acquisition, instrument control, additive manufacturing, signal processing, airborne acoustics, 3D modeling and image processing to facilitate this research. 3D models of horseshoe bat noseleaves were obtained by tomographic imaging, reconstructed, and modified in the digital domain to meet the needs of additive manufacturing prototype. Nostrils and anterior leaf were abstracted as an elliptical outlet and a concave baffle in the other prototype. As a reference, a circular outlet and a straight baffle designed. A data acquisition and instrument control system has been developed and integrated with transducers to characterize the dynamic emission system acoustically as well as actuators for recreating the dynamics of the horseshoe bat noseleaf. A conical horn and tube waveguide was designed to couple the loudspeaker to the outlet of bat noseleaf and simplified baffles. A pan-tilt was used to characterize the acoustic properties of the deforming prototypes over direction. By using those techniques, the dynamic effect of the noseleaf was reproduced and characterized. It was suggested that the lancet rotation induced both beam-gain and beamwidth changes. Narrow outlet produced an isotropic beampattern and concave baffle had a significant time-variant and frequency-variant effect with just a small displacement. All those results cast light on the possible functions of the biological morphology and provided new thoughts on the engineering device's design.

# Dedication

To my parents, for always encouraging me to study no matter in what conditions, my sister, for her endless love and support.

To my grandma, uncle and aunt, for raising me up.

To my undergraduate teacher and friend, Xuehui Li, for her unconditional love, support and encouragement.

# Acknowledgments

I would like to express my sincere thanks to my advisor, Rolf Müller. It was very fortunate for me to have such a supervisor, who always ready to help whenever I encounter difficulties and encourage me to do the best.

Thanks very much the rest of my committee members, Alexander Leonessa, Hongxiao Zhu, Nicole Abaid, Sunny Jung for their time and efforts to review the proposal and dissertation. Also, their valuable feedbacks.

I would like to thank my labmates, Anupam K Gupta, Chen Ming, Joseph Sutlive, Mingyi Liu, Philip Caspers, Syed Uzair Gilani, Yuan Lin for their discussions and support of my research.

Thanks very much the Ware Lab of Virginia Tech for machining the waveguide, Dreams Lab for printing out the elastic noseleaf prototype, Shandong University - Virginia Tech International Lab for sharing the behavior study data.

Lastly, I would like to thank the *Greater Horseshoe Bat* for inspiring this research.

# Contents

<b>1</b>	<b>Introduction</b>	<b>1</b>
1.1	Bat Biosonar & Engineered Sonar . . . . .	1
1.2	Horseshoe Bat Biosonar . . . . .	2
1.3	Dynamic Biosonar System Features . . . . .	4
1.4	Evidence for Dynamic Effects . . . . .	7
1.5	Objectives and Approach . . . . .	7
1.6	Chapter Outline . . . . .	8
<b>2</b>	<b>Methods</b>	<b>9</b>
2.1	Reproduction of Noseleaf . . . . .	9
2.2	Waveguides . . . . .	10
2.3	Baffle Curvature . . . . .	13
2.4	Prototype Manufacturing . . . . .	15
2.5	Actuation Mechanisms . . . . .	16
2.6	Acoustic Measurements . . . . .	16
2.7	Signal Processing . . . . .	20
<b>3</b>	<b>Results</b>	<b>23</b>
3.1	Waveguide Geometry . . . . .	23
3.2	Lancet Bending . . . . .	28
3.3	Outlet Geometry . . . . .	29
3.4	Baffle Geometry . . . . .	31

3.5	Static Characterization of Straight Baffle . . . . .	32
3.6	Static Characterization of Concave Baffle . . . . .	35
3.7	Dynamic Characterization of Concave Baffle . . . . .	38
<b>4</b>	<b>Discussions</b>	<b>41</b>
4.1	Interpretation of Results . . . . .	41
4.2	Relevance to Bat Biosonar . . . . .	45
4.3	Relevance to Engineering . . . . .	46
<b>5</b>	<b>Summary</b>	<b>48</b>
5.1	Major Findings . . . . .	48
5.2	Suggestions for Future Work . . . . .	49
	<b>Bibliography</b>	<b>50</b>

# List of Figures

1.1	Noseleaf morphology of the greater horseshoe bat ( <i>Rhinolophus ferrumequinum</i> ) : a) photograph of a noseleaf (frontal view), b) rendering of a digital noseleaf model. The different noseleaf parts are: 1) lancet, 2) sella, 3) anterior leaf. . . . .	4
1.2	Deformation pattern and numerical study of the lancet of the greater horseshoe bat ( <i>Rhinolophus ferrumequinum</i> ): a) high-speed video recording sequences of lancet movement, b) time window of the emission pulse period and lancet motion, c) simulation results of the lancet bending effect on the beampattern. Reproduced from [86]. . . . .	6
1.3	Deformation pattern of the anterior leaf of the greater horseshoe bat ( <i>Rhinolophus ferrumequinum</i> ): a) anterior leaf motion detected by laser, b) anterior leaf twitch motion pattern, c) simultaneous sound pressure, anterior leaf movement velocity and displacement measurements. Reproduced from [87]. . . . .	6
1.4	Typical workflow of the biosonar research. . . . .	8
2.1	Digital model and physical replica of noseleaf of the greater horseshoe bat ( <i>Rhinolophus ferrumequinum</i> ): a) original digital model, width 1 cm, height 2 cm, b) symmetric smooth model, c) physical elastic noseleaf of (b) generated by additive manufacturing (scaled 2x). The dashed line in (a) indicates the cut plane for mirroring the right half of the noseleaf to get the symmetric noseleaf. All were presented in the frontal view. . . . .	10
2.2	Cross-section of the tested waveguides: the waveguide consists of a conical horn and a circular tube, the mouth diameter of horn was always fixed to the diameter of the loudspeaker membrane (5 cm), the arrows indicate the sound radiation direction of the loudspeaker. Different combinations of horn and tube were tested in the experiment: a) horn length 4 cm, tube length 16 cm, b) horn length 7 cm, tube length 13 cm, c) horn length 11 cm, tube length 9 cm, d) horn length 15 cm, tube length 5 cm, e) horn length 20 cm. Horn mouth diameter: 5 cm, throat diameter: 7 mm, tube diameter: 7 mm. Horn length was measured in the axial direction. . . .	12

2.3	Nostril and anterior leaf cross-section of the greater horseshoe bat ( <i>Rhinolophus ferrumequinum</i> ): a) rendering of a digital noseleaf model, the dashed line indicates the position to get the cross-section of the anterior leaf, b) cross-section of the nostril, c) cross-section of the anterior leaf, the arrows indicate the sound radiation direction of the nostril. . . . .	14
2.4	Tested sound outlets and simplified dynamic baffle prototypes: a) planar outlet with circular cross-section (frontal view), b) planar outlet with elliptical cross-section (frontal view), c) baffle with straight flanks mounted on an elliptical outlet (side view), d) baffle with concave flanks mounted on an elliptical outlet (side view). The circular and elliptical outlets have cross-sectional areas of $\approx 79 \text{ mm}^2$ and approximately $12 \text{ mm}^2$ respectively. Both the straight and concave flanks have the same width 15 mm. The dashed lines indicate the semiangle of the baffle opening (shown here is a semiangle of $60^\circ$ ). . . . .	15
2.5	Typical components of the acoustic measurements: sound generation and propagation, data acquisition, prototype orientation and actuation. . . . .	17
2.6	Experimental setup for characterization of the dynamic noseleaf: 1) ultrasonic loudspeaker, 2) conical waveguide, 3) Styrofoam, 4) noseleaf (Figure 2.1c), 5) linear actuator, 6) frame, 7) pan-tilt unit. . . . .	18
2.7	Experimental setup for characterization of the dynamic baffles: 1) dynamic baffle (shown here is a straight baffle, Figure 2.4c), 2) conical waveguide, and 3) ultrasonic loudspeaker mounted on a 4) pan-tilt unit. . . . .	19
2.8	Signal processing for radiation pattern: a) acquired time domain signal was transformed into b) frequency domain by using Fourier transform, for one selected frequency (black vertical straight line in (b)) from 30 kHz to 40 kHz, the gain was plotted over full scanning space (azimuth: $-90^\circ$ to $90^\circ$ , elevation: $-30^\circ$ to $90^\circ$ ) to get the c) 2D beampattern or just over the horizontal space (azimuth: $-90^\circ$ to $90^\circ$ , elevation $0^\circ$ , red horizontal line in (c)) to get the d) 1D beampattern. . . . .	21
2.9	Signal processing for the dynamic concave baffle: for one selected frequency from 30 kHz, 40 kHz and 50 kHz, the envelope of time domain data (blue in (a), (b), (c)) was extracted by using Hilbert transform and plotted over position (example: a) $30^\circ$ , b) $0^\circ$ , c) $-60^\circ$ ) to get the d) time variant signature. Inset in (b) shows the detailed envelope pattern. . . . .	22

3.1	Effect of throat diameter for different horn axial lengths on the on-axis far-field pressure: conical horns with the same mouth diameter (5 cm), different throat diameters (blue: 7 mm and magenta: 3 mm) and various horn axial lengths ( b: 4 cm, c: 10 cm, d: 15 cm) were tested. The inset (a) shows the horn cross section and the arrows indicate the sound radiation direction of the loudspeaker. The red solid line and dashed line shows the loudspeaker and noise pressure response respectively. Interested frequency (30 kHz-40 kHz) range was marked by black dashed line. . . .	24
3.2	Effect of waveguide horn axial length on the on-axis far-field pressure: conical horn and circular tube waveguides with the same mouth diameter (5 cm), throat diameter (7 mm), tube length (8 cm) and different horn axial lengths (magenta: 4 cm, green: 10 cm, blue: 15 cm) were tested. The inset shows the conical horn and circular tube waveguide cross section and the arrows indicate the sound radiation direction of the loudspeaker. Red solid line and dashed line shows the loudspeaker and noise pressure response respectively. Interested frequency range (30 kHz-40 kHz) was marked by black dashed line. . . . .	25
3.3	Effect of waveguide tube length on the on-axis far-field pressure: conical horn and circular tube waveguides with fixed mouth diameter (5 cm), throat diameter (7 mm), horn axial length (10 cm) and different tube lengths (magenta: 4 cm, green: 8 cm, blue: 12 cm) were tested. The inset shows the conical horn and circular tube waveguide cross section and the arrows indicate the sound radiation direction of the loudspeaker. Red solid line and dashed line shows the loudspeaker and noise pressure response respectively. Interested frequency range (30 kHz-40 kHz) was marked by black dashed line. . . . .	26
3.4	Effect of horn axial length and tube length ratio on the on-axis far-field pressure: two different conical horn and circular tube waveguides with the same mouth diameter (5 cm) and throat diameter (7 mm) were tested (blue: horn axial length 4 cm, tube length 16 cm, ratio 0.2; magenta: horn axial length 15 cm, tube length 5 cm, ratio 0.8. Here just shows two examples of Figure 2.2). The top inset shows the conical horn and circular tube waveguide cross section and the arrows indicate the sound radiation direction of the loudspeaker. Red solid line and dashed line shows the loudspeaker and noise pressure response respectively. Interested frequency range (30 kHz-40 kHz) was marked by black dashed line. . . . .	27
3.5	Beampatterns at various bending stages of the noseleaf replica: for each experimental repetition (a and b), the lancet was bent from 0° to 5° in steps of 1°, frequencies range from 30 kHz (corresponds to 60 kHz in bats) to 38 kHz (corresponds to 76 kHz in bats) in steps of 4 kHz. Experiment setup was showed in Figure 2.6 and signal processing method was showed in Figure 2.8. . . . .	28

3.6	Influence of circular outlet diameter on the beampatterns: a) 30 kHz, b) 32 kHz, c) 34 kHz, d) 36 kHz e) 38 kHz, f) 40 kHz. Circular outlets with different diameters (green: 2 mm, magenta: 6 mm, blue: 10 mm) were tested. Signal processing method was showed in Figure 2.8. . . . .	30
3.7	Influence of elliptical outlet on the beampatterns: a) 30 kHz, b) 32 kHz, c) 34 kHz, d) 36 kHz e) 38 kHz, f) 40 kHz. Elliptical outlets with the same major axis (red: 15 mm) and different minor axes (black: 3 mm, cyan: 1 mm) were tested. Signal processing method was showed in Figure 2.8. . . . .	30
3.8	Beampattern effects due to the length of the straight baffle: different baffle lengths (b, 1 cm; c, 2 cm) and different baffle semiangles (blue: 60°, red: 30°) were tested at various frequencies: 30 kHz, 34 kHz, 38 kHz. The dashed lines indicate the semiangle of the baffle opening (inset a, shown here is a semiangle of 60°). Experiment setup was showed in Figure 2.7, beampattern was measured along the minor axis (1 mm) of the elliptical outlet. Signal processing method was showed in Figure 2.8. . . . .	32
3.9	Beampattern effects due to static bending of the straight baffle: a) reference opening angle was 90° and bending angle varied, b) root-mean-square gain difference between beampatterns produced by a 90°-reference and a tested opening angle, all rms differences were computed with averaging over 21 frequencies ranging from 30 kHz to 40 kHz in steps of 0.5 kHz as well as over angle, black straight line shows the linear regression between the bending angle and the median (blue dot) of the rms difference, slope 0.05 dB/°, coefficient of determination $r^2 = 0.97$ , c) example beampatterns shown are for a frequency of 34 kHz of different baffle opening angles: 90°(black), 80°(blue), 70°(green), 60°(cyan), 50°(magenta), 40°(red), 30°(purple). In the box-and-whisker plots, the whiskers denote the location of the minimum and maximum, the edges of the box the first and third quartiles, and the horizontal line the median. Experiment setup was showed in Figure 2.7, beampattern was measured along the minor axis (1 mm) of the elliptical outlet. Signal processing method was showed in Figure 2.8. . . . .	34
3.10	Beampattern effects due to static bending of the concave baffle: a) root-mean-square gain difference between beampatterns produced by a 90°-reference and a tested opening angle (Figure 3.9a), all rms differences were computed with averaging over 21 frequencies ranging from 30 kHz to 40 kHz in steps of 0.5 kHz as well as over angle, b) example beampatterns shown are for a frequency of 34 kHz of different baffle opening angles: 90° (black), 80° (blue), 70° (green), 60° (cyan), 50° (magenta), 40° (red), 30° (purple). In the box-and-whisker plots, the whiskers denote the location of the minimum and maximum, the edges of the box the first and third quartiles, and the horizontal line the median. Experiment setup was showed in Figure 2.7, beampattern was measured along the minor axis (1 mm) of the elliptical outlet. Signal processing method was showed in Figure 2.8. . . . .	37

3.11	Beam pattern effects due to static bending of the concave baffle over small angles ( $0^\circ$ to $10^\circ$ ). Root-mean-square gain difference between beam patterns produced by a $90^\circ$ -reference and a tested opening angle (Figure 3.9a). The reference opening angle was $90^\circ$ for all conditions (Figure 3.9a). Black straight line shows the linear regression between the bending angle (from $3^\circ$ to $10^\circ$ ) and the median (blue dot) of the rms difference, slope $0.2 \text{ dB}/^\circ$ , coefficient of determination $r^2 = 0.92$ . The example beam pattern plots show beam patterns for inwards bending angles relative to the reference of (a) $3^\circ$ , (b) $5^\circ$ , and (c) $7^\circ$ . All other experimental and display parameters were the same as Figure 3.10. Experiment setup was shown in Figure 2.7, beam pattern was measured along the minor axis (1 mm) of the elliptical outlet. Signal processing method was shown in Figure 2.8. . . . .	38
3.12	Example of a continuous time-variant signature created by motion of a concave baffle: a) measurement direction relative to the baffle, b,c,d) magnitudes (envelope of the analytic signal) of signal received from the dynamic baffle for frequencies of b) 50 kHz, c) 40 kHz, and d) 30 kHz. The static reference (opening angle $60^\circ$ ) are shown in e) 50 kHz, f) 40 kHz, and g) 30 kHz. The baffle motion executed in this example ranged from $-60^\circ$ to $30^\circ$ in 250 ms. Signal was measured along the minor axis (1 mm) of the elliptical outlet. Signal processing method was shown in Figure 2.9. . . . .	40
4.1	Governing equation and examples of the far-field radiation pattern of the elliptical outlet: a) governing equation of the elliptical outlet far-field radiation pattern, $a$ is the semi-minor axis and $b$ is the semi-major axis of the elliptical outlet, $J_1$ is the first kind Bessel equation. $\theta$ is the cone angle and $\phi$ is the azimuthal angle within the elliptical outlet plane, b) elliptical outlet far-field radiation pattern of 34 kHz, minor axis length 1 mm (red), major axis length 15 mm (blue). . . . .	43
4.2	Normalized acoustic resistance of conical horn with different horn angles: $30^\circ$ (red), $40^\circ$ (green), $50^\circ$ (blue), $60^\circ$ (cyan), $70^\circ$ (black), $80^\circ$ (magenta), $90^\circ$ (purple). Inset shows the cross-section of the conical horn, throat diameter 1 mm, horn length 2 cm. . . . .	44
4.3	Bending effect of the conical horn angle on the root-mean-square (rms) gain difference between reference angle ( $90^\circ$ ) beam pattern and tested angle ( $30^\circ$ - $80^\circ$ in steps of $10^\circ$ ) beam pattern: black straight line shows the linear regression between the bending angle and the median (blue dot) of the rms difference, slope $0.2 \text{ dB}/^\circ$ , coefficient of determination $r^2 = 1$ . RMS beam-gain differences of 21 frequencies ranging from 30 kHz to 40 kHz in steps of 0.5 kHz are in each box-and-whisker plot. . . . .	45

- 4.4 A horn approximation of the anterior leaf compared to other horns: a) cross-sections of the anterior leaf (thick line, circles) compared to Bessel (stars), conical (squares), and exponential (triangles) horns, b) numerical predictions of the acoustic resistances (normalized by a plane wave over the throat area of the horns) for the horn cross-sections shown in (a). The inset in (a) shows the cutting plane through the anterior leaf that was used to obtain the anterior leaf cross-section. . . . 47

# List of Tables

3.1	Influence of the circular outlet diameter on the on-axis far-field pressure (dB SPL) for different frequencies . . . . .	29
3.2	Influence of the baffle dimension on the -6 dB beamwidth (°) for different frequencies (beampattern was measured along the minor axis of the elliptical outlet) . . . . .	31
3.3	Influence of the baffle dimension on the on-axis far-field pressure (dB SPL) for different frequencies (beampattern was measured along the minor axis of the elliptical outlet) . . . . .	31
3.4	Influence of the bending angle on the median root mean square difference for 2 cm straight baffle . . . . .	33
3.5	Influence of the bending angle on the on-axis far-field pressure response of 34 kHz for 2 cm straight baffle . . . . .	33
3.6	Influence of the bending angle on the -6 dB beamwidth of 34 kHz for 2 cm straight baffle . . . . .	33
3.7	Influence of the bending angle on the median root mean square difference for 2 cm concave baffle . . . . .	35
3.8	Influence of the small bending angle on the median root mean square difference for 2 cm concave baffle . . . . .	36

# Chapter 1

## Introduction

This chapter introduces the principles and advantages of the bat biosonar compared with the man-made sonar, provides detailed discussions of the emission and reception dynamics of the biosonar system and delivers the goals and approach of the current research.

### 1.1 Bat Biosonar & Engineered Sonar

The evolution of bats is characterized by a combination of two key innovations, powered flight and echolocation, which are unique among mammals [1, 2, 3].

Due to their flight ability, bats are distributed almost all over the world except for polar regions and small remote islands. Their food varies from small insects to large vertebrates [4] and their habitats range from narrow dense forests to large open deserts [5, 6]. Lots of attention have been directed toward to how they perceive the information of those different types of environments as well as how they acquire food in challenging circumstances, which casts light on solutions for similar engineering problems. For example, researchers reported that the nectar-feeding bats have developed highly mobile tongues to reach deep within the columnar flowers to obtain nectar [7]. It was found that the nectar-feeding bats can change the size and shape of their tongues dynamically, which could serve as a model for miniature liquid harvest robot.

Other than food acquisition problems, a volume of studies have been done regarding echolocation of bats [8]. Not all bats have the ability of echolocation. Some of the bats rely on vision or passive sensory methods [9], i.e. they get the information by making use of the sound emits from the surroundings. Even though for the active sensing bats, not all of them echolocate the same way. The active sonar system consists of emitters (mouth or nostrils) and receivers (two ears). Many of the echolocating bats produce the ultrasound in the larynx, emit the sound from the mouth or nose and use the external ears to receive the echoes. Information is obtained by analyzing the echoes to get the target properties, such as distance, angle and texture [10, 11, 12, 13]. The size of mouth or

the nostrils and the ears do not differ much from the wavelengths they used. The ears of bats, for example, do not exceed a few centimeters in length [14] while the smallest received wavelengths are still a few millimeters [15, 16]. Hence, the minimum ratio between ear size and wavelength does not fall below  $10^{-1}$ . In contrast to this, technical sonar arrays are typically 100 or even 1000 times larger than the wavelength they operate on [17, 18, 19].

Even though the echolocating bats have those simple biosonar elements and small size-to-wavelength ratio, the performance of their sonar systems outperform the current state-of-art engineering sonar systems in a variety of ways [20].

First of all, depending on the sensory needs, echolocating bats can actively control the parameters of the emitting sound, such as intensity, duration, bandwidth and repetition rate [21, 22]. It was pointed out that during the final stage of the bat hunting activity, the sound repetition rate increased [23] and can reach to 220 Hz [24]. The superfast laryngeal muscle enables them to do so [25]. Accompanied with a high repetition rate, the pulse duration was decreased [26]. Those robust call design and waveform diversity in bats could be used in the current radar and sonar systems to assist tasks such as autonomous navigation and target classification [27].

Second, echolocating bats have a mature spatial orientation ability regardless of the relatively wide sonar beam they used. Operation in a regime where device size exceeds wavelength by two or more orders of magnitude allows engineered sonar and radar systems to gather sensory information on the environment through scans with narrow beam arrays [28, 29]. In their very different size-to-wavelength regime, bats are very poorly suited for this paradigm. Indeed, bats used comparatively wide beamwidth with reported values ranging from  $28^\circ$  to  $80^\circ$  (full width at -6 dB) [30, 31, 32, 33, 34, 35]. For example, in the greater horseshoe bat, the -6 dB beamwidth is  $48^\circ$  elevation and  $46^\circ$  azimuth [32]. Yet, despite their wide beams, bats are able to navigate and pursue their prey in structure-rich natural environments [36, 37, 38, 39]. Take greater horseshoe bat for example, it was found that the bats could detect echoes from the fluttering insects even in a cluttered environment [40].

At last, the effectiveness and efficiency of the man-made sonar highly depend on the current technology [41, 42] while biosonar has more flexibility. For example, in the man-made sonar, the properties of the transducers influence the waveforms they generate [42].

In the process of time, bats have developed a sophisticated active sonar system to survive, which need to be better understood and then utilized to improve the current engineering sonar systems or design them from the ground up.

## 1.2 Horseshoe Bat Biosonar

According to their time-frequency structure, the emission pulses can be divided into two components: constant frequency (CF) and frequency modulation (FM). Horseshoe bats are FM-CF-FM [43, 44] and high duty cycle echolocators [16]. In those bats, sound emission and reception hap-

pens at the same time, thus they need to separate the calls and echoes in frequency. The sound they emit from the nostrils (rather than from mouth) consists of three parts, a short frequency modulated (FM) upward sweep at the beginning, a long constant frequency (CF) part and a brief FM downward sweep at the end. In the greater horseshoe bat, the frequency range of the sound they emit is 60 kHz-80 kHz (2nd harmonic). The morphology and acoustic functions of the ear and noseleaf are associated with those echolocation features.

On the reception side, the general shape of ear could be approximated as a truncated conical horn [45, 46, 47], the dimension of the ear is correlated with the emission frequency [14] and the local features, such as flaps in the pinna wall, tragus and antitragus in the pinna rim, folds between the pinnae [48, 49, 50], play an important role in beamforming. Obviously, the pinna itself determines interaural level differences (ILD) and the ear's sensitivity to echoes [51, 52, 53, 54, 55, 56]. Object discrimination experiment [57], prey capture performance experiment [58] and numerical simulation [59] all showed that the tragus aids the vertical localization of the bat. Removing the flap in the pinna wall induces a decrease of the directional information, which indicates that the present of the flap improves the spatial information [60]. Even the small ridges in the pinna wall and the skin folds between the pinnae have a narrowing effect on the beampattern [61, 62].

While one can find ears in all bats, noseleaves are found across several large and diverse bat families such as Old World leaf-nosed bats (Hipposideridae), New World leaf-nosed bats (Phyllostomidae) and horseshoe bats (Rhinolophidae) [63, 64, 65]. In the greater horseshoe bat (*Rhinolophus ferrumequinum*), the complex noseleaf consists of three distinguished parts [66, 67] (Figure 1.1):

- 1) lancet, located right above the nostrils and has several furrows in it;
- 2) sella, a protrusion extending from the lancet plane;
- 3) anterior leaf, a horseshoe-shaped plate closely around the two nostrils.

Like the ear, the dimension of the noseleaf is correlated with the emission frequency [68], which indicates that the noseleaf is related with acoustic function. A behavior study demonstrated that if the upper part of the noseleaf was covered with petroleum jelly, the beampattern became not smooth [32]. This case is hard to explain whether the noseleaf itself has impact on the beampattern as there are hairs in the noseleaf surface. But direct evidence showed that the noseleaf is a kind of functional structure: bending the lancet back increased the vertical beamwidth [69]. Moreover, numerical simulation showed that the furrows in the lancet acted as resonators, which resulted in a narrower sonar beam [70, 71, 72, 73]. The sella and the anterior leaf also has the function of focusing the sonar beam [71, 74].

All in all, the horseshoe bat has a sophisticated active sonar system with complex sound diffraction structures.

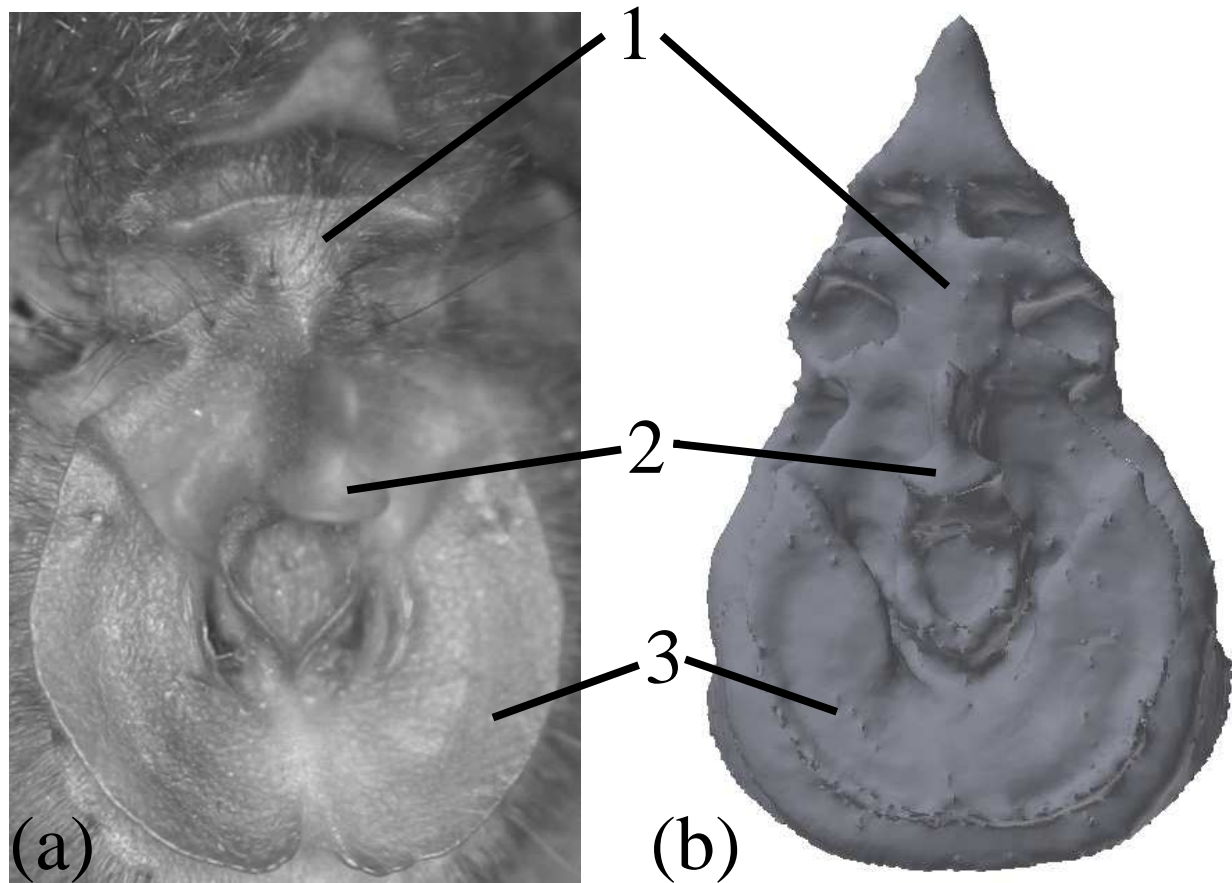


Figure 1.1: Noseleaf morphology of the greater horseshoe bat (*Rhinolophus ferrumequinum*): a) photograph of a noseleaf (frontal view), b) rendering of a digital noseleaf model. The different noseleaf parts are: 1) lancet, 2) sella, 3) anterior leaf.

### 1.3 Dynamic Biosonar System Features

It was still unclear which factor contributed to the high performance of biosonar, but it was hypothesized that the high performance was at least due to the bats' dynamic periphery of their sophisticated sonar systems. The sonar systems in bats, i.e., the ears and noseleaves, are not static features and they can undergo non-rigid deformations.

The pinna movements were first discovered in the greater horseshoe bat (*Rhinolophus ferrumequinum*) [75]. Some of the bats hold their ears fixed in the space relative to their head position, but others move them in various ways, such as the greater horseshoe bat mentioned before. Other than independent movement, the ears also move simultaneously. Those movements are controlled by ear muscles [75]. One group of the muscles enable the rigid rotation of the ear, the other group is in charge of non-rigid deformation. The maximum displacement of the ear tip was more than

4 mm, which is comparable with the wavelength of the constant frequency (80 kHz) component of the emit sound. More interestingly, the ear alternating movements were closely related to the sound emission [76, 77, 78, 79, 80]. When bats are interested in things close by, one ear moves forward and the other ear moves backward rapidly while emitting the buzz pulse, which is highly consist. If the ear movements were disabled by cutting the nerves and muscles, the obstacle avoidance performance of the vertical target localization degraded while the ability of the horizontal target localization remained intact [81]. Further, numerical simulation showed that during the non-rigid deformation sequences, the sensitivity of the main lobe of the beampattern remained almost constant. On the contrary, the sensitivity of the side lobe increased [82]. A smart reception dynamic baffle was designed based on all those acoustic effects of the ear structures [83]. When implemented the local ear features (ridges, incision, antitragus) into an obliquely truncated cone separately, there was no significant effect on the beampattern. If one combined all those local features, stronger sidelobes appeared, which quantitatively agreed with the simulation results and indicated that the local ear features have a higher degree of system integration [50]. In addition, it was suggested that the biomimetic dynamic sound reception baffle had a significant time-variant effect [84].

Later, similar non-rigid dynamics were also observed on the emission side. The structures associated with the noseleaf, such as lancet and anterior leaf can undergo non-random motions with specific muscular control [85]. Those motions are not a byproduct of physiological activities, the bats can actively control the motion and switch it on an off [86, 87]. The lancet can bend forward and recover backward during the sound emission period (Figure 1.2a,b). The maximum rotation of the lancet can reach to  $12^\circ$  and the average linear displacement was less than 1 mm. As the lancet was bent, sidelobes were generated at low frequencies, while it didn't has a big effect on the beam-pattern at high frequencies (Figure 1.2c) [86, 73]. Compared with the lancet, the anterior leaf of the noseleaf can twitch inward and forward, thus changing the curvature of the horseshoe-shaped plane (Figure 1.3) and finally diffracting the outgoing waves [87]. The average distal and proximal displacement of the anterior leaf was around 0.4 mm. Even though the displacement was small, it was notable compared with the size of the noseleaf and the emission wavelengths (4 mm-6 mm). A biomimetic prototype was developed in order to reproduce the emission dynamics observed in bats [88, 89, 90].

Up to now, many details of emission dynamics still have to be characterized to better understand the principle behind those dynamic features.

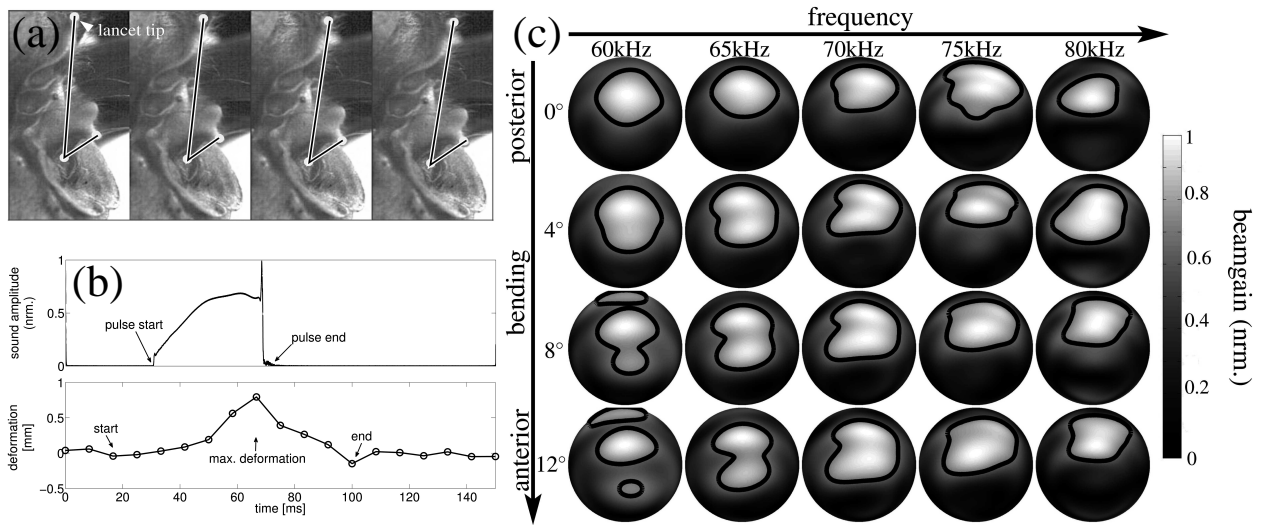


Figure 1.2: Deformation pattern and numerical study of the lancet of the greater horseshoe bat (*Rhinolophus ferrumequinum*): a) high-speed video recording sequences of lancet movement, b) time window of the emission pulse period and lancet motion, c) simulation results of the lancet bending effect on the beam pattern. Reproduced from [86].

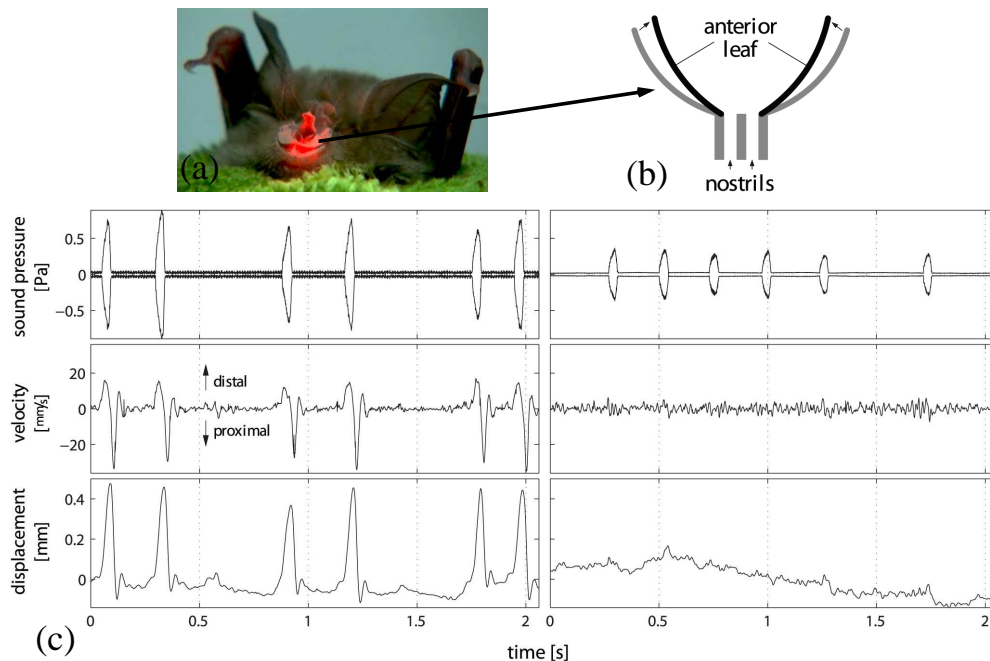


Figure 1.3: Deformation pattern of the anterior leaf of the greater horseshoe bat (*Rhinolophus ferrumequinum*): a) anterior leaf motion detected by laser, b) anterior leaf twitch motion pattern, c) simultaneous sound pressure, anterior leaf movement velocity and displacement measurements. Reproduced from [87].

## 1.4 Evidence for Dynamic Effects

The dynamic system features could have an influence on the acoustic function: many evidences showed that bats can change their emission beamwidth under certain circumstances to control their field of view [91, 92, 93, 94, 95, 96]. Adaptive beamwidth control was observed both in the Vespertilionid bats (*Myotis daubentonii*) and horseshoe bats (*Rhinolophus ferrumequinum nippon*) [91, 93]. When those two kind of bats approached the prey, the width of the emission beam increased compared with the initial hunting phase. By doing so, the bat can increase the prey capture performance. In the case of prey escaping, the bat can still have the chance to recapture the prey due to the larger field of view. In the Vespertilionid bats, by lowering the emit frequency, the beamwidth got wider [91]. Since the Vespertilioind bats emit the sound from the mouth, by changing the size of mouth, the beamwidth also changed [95]. But, for the horseshoe bats, they didn't change the frequency in their buzz phase [93], which suggested that the horseshoe bats implement other methods to change the beamwidth. Since the beamwidth depends on the relationship between the wavelength and the aperture size [97] and the horseshoe bats emit the ultrasound from the nose, it was hypothesized that changing the curvature of the noseleaf could induce the beamwidth change, which needs experimental verification and validation.

## 1.5 Objectives and Approach

From behavioral study point of view, acoustic function of the noseleaf could be obtained by directly investigating the live bat unless the experimental subject cooperates sustainability. In order to make the problem easy to handle, experimental approach was used.

The objectives of this research are (Figure 1.4):

- 1) design a dynamic emission baffle based on the horseshoe bat noseleaf;
- 2) design an experimental setup which can continuously control the baffle;
- 3) investigate acoustic effects of the dynamic emission baffle and
- 4) understand how biology sonar system works and give insights into the engineering sonar design.

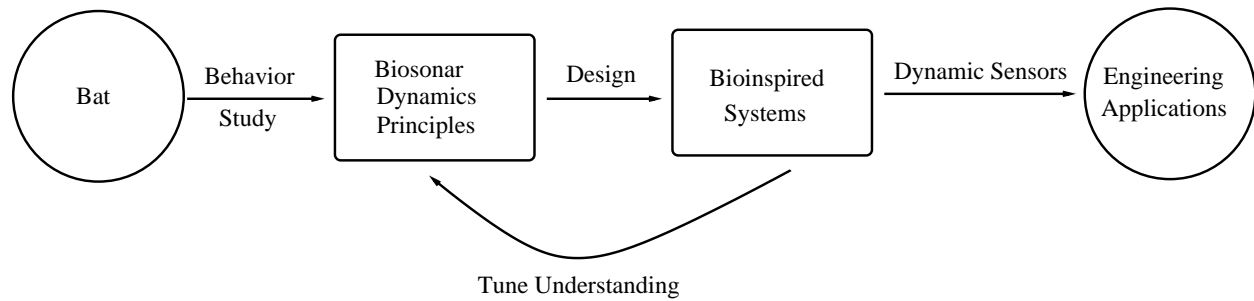


Figure 1.4: Typical workflow of the biosonar research.

## 1.6 Chapter Outline

The remaining parts of the thesis are arranged as follows:

*Chapter 2* describes the designed emission prototypes, the data acquisition setup and the digital signal processing techniques.

*Chapter 3* presents the static and dynamic characterization of the emission baffle.

*Chapter 4* discusses the principles behind the experimental results.

*Chapter 5* summarizes the current research and suggests the future research directions.

# Chapter 2

## Methods

Two prototypes were proposed, i.e. intact noseleaf and simple noseleaf, based on the biological morphology of the greater horseshoe bat (*Rhinolophus ferrumequinum*).

In order to allow the prototypes to mimic the correlated behavior between the sound emission and the dynamic baffle motion, an automated experimental setup was designed.

Both the time domain and frequency domain signal processing methods were used to investigate the dynamic effect of the prototypes.

### 2.1 Reproduction of Noseleaf

The biomimetic prototype designed here was in an attempt to preserve the original features of the noseleaf. To meet this need, digital image processing and additive manufacturing methods were adopted.

The studied intact noseleaf model came from the greater horseshoe bat (*Rhinolophus ferrumequinum*), which was captured in caves near Jinan, Shandong, China [86].

In an effort to get the physical replica of the noseleaf, the following manufacturing procedure (Figure 2.1) was implemented:

1. the  $\mu$ CT (Skyscan 1072) was used to get the digital model from the fresh died bat, the width of the noseleaf is 1 cm and the height is 2 cm;
2. the noseleaf was cut through the mid-plane and the right half was mirrored to get the symmetric noseleaf (software: Zbrush), thus the acoustic effect of the asymmetric structure was eliminated;
3. the surface of the symmetric noseleaf model was smoothed (software: Zbrush) in order to get rid of the roughness effect;

4. the noseleaf was fabricated through additive manufacturing technique (Objet Connex 350, serial number 35019) by using elastic material (Objet TangoBlackPlus FullCure980).

As mentioned before, the width of the noseleaf is about 1 cm, which is hard to handle. In order to allow more freedom to manipulate the noseleaf, the prototype size was scaled two times than the original size of the noseleaf. Correspondingly, the interested frequency range one should look into was 30 kHz to 40 kHz on the ground of size-frequency relationship [68]. On the contrary, the thickness was not scaled since it was believed that the thickness of the material plays no role in the acoustic function [98].

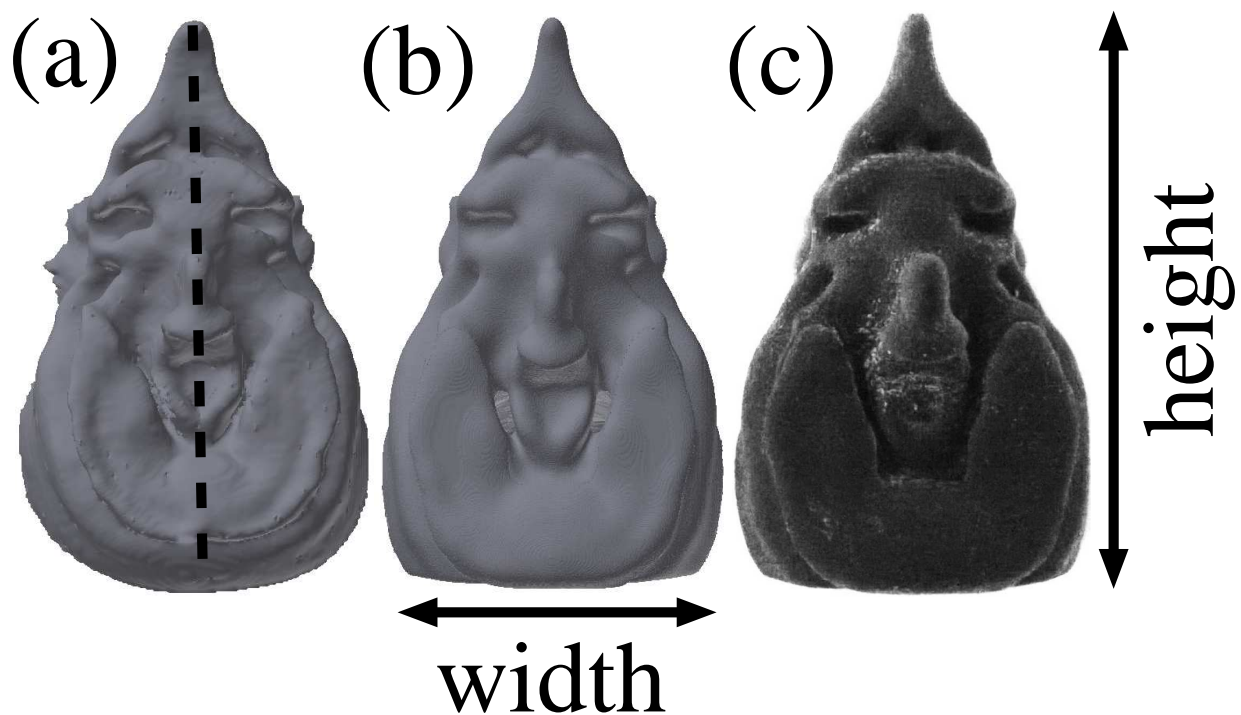


Figure 2.1: Digital model and physical replica of noseleaf of the greater horseshoe bat (*Rhinolophus ferrumequinum*): a) original digital model, width 1 cm, height 2 cm, b) symmetric smooth model, c) physical elastic noseleaf of (b) generated by additive manufacturing (scaled 2x). The dashed line in (a) indicates the cut plane for mirroring the right half of the noseleaf to get the symmetric noseleaf. All were presented in the frontal view.

## 2.2 Waveguides

Since the available ultrasonic loudspeaker (Ultra Sound Advice S56 with Ultra Sound Advice S55 amplifier) had a larger dimension of sound source (diameter 5 cm) than the narrow nostrils, a conical horn and circular tube waveguide was brought up to make up this dimension difference.

The conical horn was always attached to the loudspeaker. The part of conical horn next to the loudspeaker is called "mouth" and the narrow outlet far away from the loudspeaker is called "throat".

Different kinds of waveguide were tested to investigate the geometry effect on the gain and pattern of the on-axis far-field frequency response:

1. conical horn of different axial lengths (4 cm, 10 cm, 15 cm), different throat diameters (3 mm, 7 mm) and fixed mouth diameter 5 cm were used to investigate acoustic effect of the horn axial length and throat diameter;
2. conical horn and circular tube waveguide with different horn axial lengths and tube lengths (total horn axial length and tube length is 20 cm, Figure 2.2), fixed horn mouth diameter 5 cm, throat diameter 7 mm and tube diameter 7 mm were used to study acoustic effect of the ratio between the horn axial length and tube length.

A calibrated microphone (Brüel and Kjør 4138-1/8" pressure-field microphone with Brüel and Kjør NEXUS 2690-A-0S1 1-channel Microphone Conditioning Amplifier) was placed in the far field (1 m away from the loudspeaker) to measure the frequency response of the waveguides.

The desired conical horn and circular tube waveguide is the one which can maintain a sufficient signal-to-noise ratio as well as produce a smooth (no big peaks and valleys) on-axis far-field frequency response.

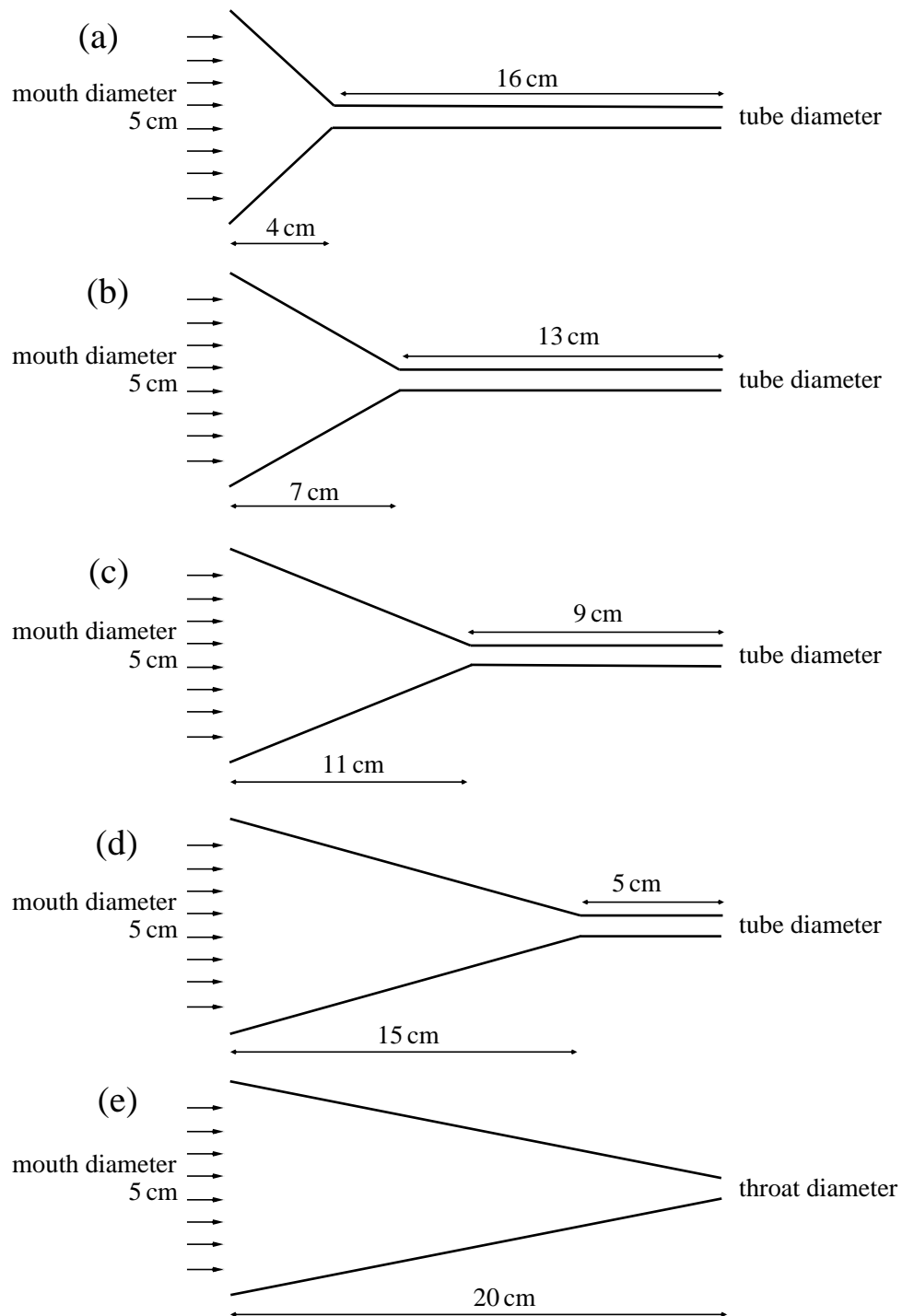


Figure 2.2: Cross-section of the tested waveguides: the waveguide consists of a conical horn and a circular tube, the mouth diameter of horn was always fixed to the diameter of the loudspeaker membrane (5 cm), the arrows indicate the sound radiation direction of the loudspeaker. Different combinations of horn and tube were tested in the experiment: a) horn length 4 cm, tube length 16 cm, b) horn length 7 cm, tube length 13 cm, c) horn length 11 cm, tube length 9 cm, d) horn length 15 cm, tube length 5 cm, e) horn length 20 cm. Horn mouth diameter: 5 cm, throat diameter: 7 mm, tube diameter: 7 mm. Horn length was measured in the axial direction.

## 2.3 Baffle Curvature

Different than the biomimetic prototype, the bioinspired baffle prototype developed here was to simplify the complicate structure of the noseleaf while the important functional features of the noseleaf were preserved.

The basic geometry of the bioinspired baffle prototype was motivated by the biological morphology of the nostrils and anterior leaf. Attentive examination of noseleaf of the greater horseshoe bat (*Rhinolophus ferrumequinum*) showed that the nostril cross-section is not circular, which is narrow in the radial direction (diameter  $\sim 0.5$  mm) and wide in the orthogonal direction (diameter 3 mm) with curve transition (Figure 2.3b). Additionally, It was found that the shape of the baffle closely surrounding the nostrils, which is called anterior leaf, is neither convex nor straight but concave (Figure 2.3c).

Based on the above observations, an elliptical outlet (major axis length 15 mm, minor axis length 1 mm, approximately 12 mm<sup>2</sup> area, Figure 2.4b) was constructed to mimic the narrow nostril aperture. The outlet flanged with concave baffles (width 15 mm, length 20 mm, Figure 2.4d) was used to model the anterior leaf.

As a control to the model baffle, circular outlets with different diameters (2 mm, 6 mm and 10 mm, Figure 2.4a) and elliptical outlet flanged with straight baffles of different axial lengths (10 mm, 20 mm, Figure 2.4c) were constructed.

The width of baffles was the same as the major axis of elliptical outlet (15 mm).

A conical horn (axial length 10 cm, mouth diameter 5 cm and throat diameter 1 cm) and nonuniform tube (length 5 cm) waveguide was used to couple the loudspeaker and the baffles. The mouth of the conical horn was connected with the loudspeaker and the throat was interfaced with on end of the tube (circular cross-section, diameter 1 cm), the other end of the tube had an elliptical cross-section (major axis length 15 mm, minor axis length 1 mm), where the baffles were attached perpendicular to the major axis. The whole assembly was mounted on a pan-tilt unit (FLIR Motion Control System PTU-D48E), which scanned 180° horizontally (azimuth: -90° to 90°, elevation: 0°) with 3° angular resolution.

A calibrated microphone (Brüel and Kjør 4138-1/8" pressure-field microphone with Brüel and Kjør NEXUS 2690-A-0S1 1-channel Microphone Conditioning Amplifier) was placed in the far field (1 m away from the loudspeaker) to measure the radiation pattern of the outlets and baffles.

The radiation pattern was used to figure out which outlet geometry will give an omnidirectional beampattern, which baffle dimension will produce obvious beampattern change and how the baffle shape as well as baffle angle changes the far-field radiation pattern.

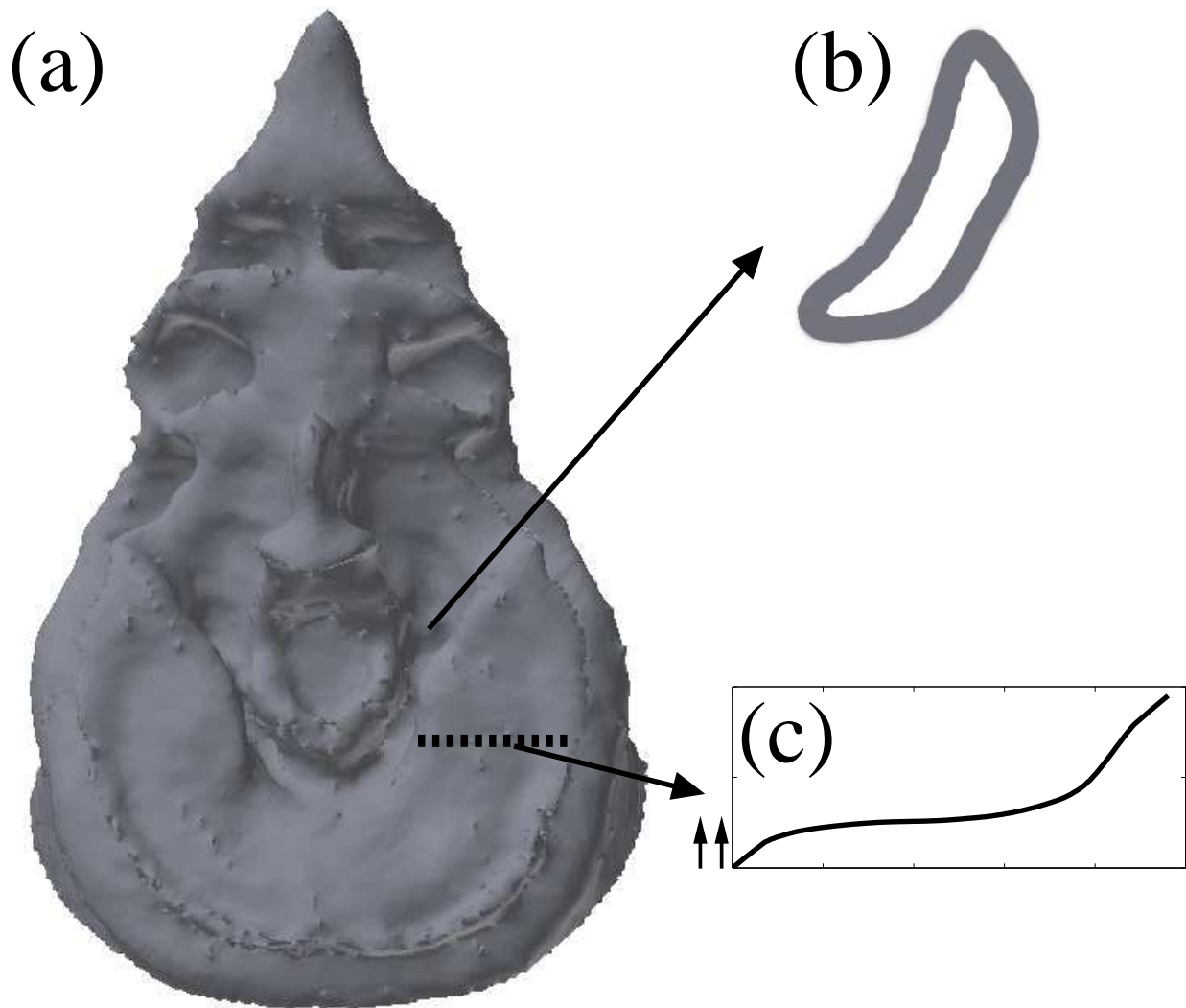


Figure 2.3: Nostril and anterior leaf cross-section of the greater horseshoe bat (*Rhinolophus ferrumequinum*): a) rendering of a digital noseleaf model, the dashed line indicates the position to get the cross-section of the anterior leaf, b) cross-section of the nostril, c) cross-section of the anterior leaf, the arrows indicate the sound radiation direction of the nostril.

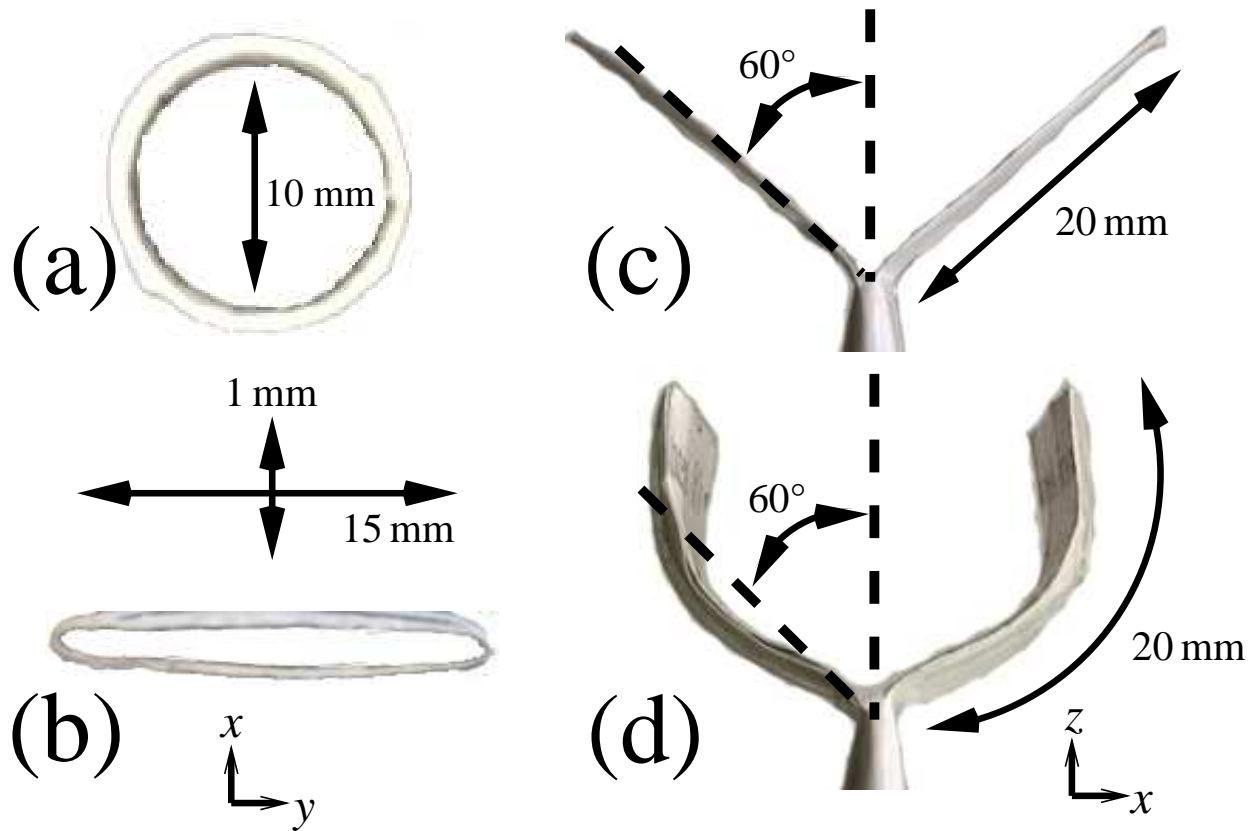


Figure 2.4: Tested sound outlets and simplified dynamic baffle prototypes: a) planar outlet with circular cross-section (frontal view), b) planar outlet with elliptical cross-section (frontal view), c) baffle with straight flanks mounted on an elliptical outlet (side view), d) baffle with concave flanks mounted on an elliptical outlet (side view). The circular and elliptical outlets have cross-sectional areas of  $\approx 79 \text{ mm}^2$  and approximately  $12 \text{ mm}^2$  respectively. Both the straight and concave flanks have the same width 15 mm. The dashed lines indicate the semiangle of the baffle opening (shown here is a semiangle of  $60^\circ$ ).

## 2.4 Prototype Manufacturing

The manufacturing process of the biomimetic prototype was shown before.

The bioinspired baffles, including the outlets, were made of paper. By squeezing the circular outlet, one can get the elliptical outlet.

During the initial testing stage, the waveguides were made of paper. Once the desired dimension was set, the waveguide was machined from the Aluminum by using CNC method.

## 2.5 Actuation Mechanisms

Different actuation configurations were applied to the prototypes based on the available actuators and the experimental feasibility. Both prototypes were actuated by the same actuation mechanism: point actuation.

For the biomimetic prototype, two linear actuators (Firgelli L12-1) were used to deform the nose-leaf. One actuator was used to bend the lancet while the other was used to move the anterior leaf through thin rod.

The maximum speed of the linear actuator is 23 mm/s, maximum stroke is 30 mm and maximum side force is 40 N. The linear actuator weights 34 grams [99].

For the bioinspired baffle, angle template was used to determine the static bending angle and a single actuator (Hitec digital servomotor HS-225BB Mighty Mini) was used to move the baffle continuously through thin rod too.

The maximum speed of this actuator is 545 %s and maximum torque is 0.5 Nm. The weight of the actuator is 27 grams [100].

## 2.6 Acoustic Measurements

The implemented experimental setup had the following capabilities: signal generation and propagation, data acquisition, prototype orientation and actuation. All those functions were integrated into a single automated setup (Figure 2.5).

The loudspeaker (Ultra Sound Advice S56, diameter 5 cm with Ultra Sound Advice S55 amplifier) sent out the linear-frequency modulated chirp signal (duration 2 ms, 10 kHz-100 kHz, gated by raised-cosine flanks), which traveled through the waveguide, was modulated by different prototypes and a calibrated microphone (Brüel and Kjær 4138-1/8 " pressure-field microphone with Brüel and Kjær NEXUS 2690-A-0S1 1-channel Microphone Conditioning Amplifier) captured the signal in the far-field about 1 m away from the loudspeaker. The recorded signal was digitized by a PXI data acquisition system (National Instruments PXIe-1073 chassis with PXIe-6356 X series multifunction data acquisition card) at a sampling rate of 1 MHz and resolution of 16 bits.

In the biomimetic noseleaf setup (Figure 2.6), the two linear actuators (Firgelli L12-1) were housed in an enclosure below the waveguide (horn axial length 10 cm, mouth diameter 5 cm, throat diameter 7 mm, tube length 10 cm, tube diameter 7 mm) and behind the noseleaf, thus the acoustic parts and electrical parts were not influence each other. The noseleaf was fixed on an artificial head consisting of a Styrofoam hemisphere, which allows for stability of the noseleaf, blocks actuator noise and directs reflections away from the noseleaf [88, 89].

In the bioinspired baffle setup (Figure 2.7), one end of the tube (tube length 5 cm) had a circular cross-section (diameter 1 cm), which was interfaced with the conical horn (axial length 10 cm,

mouth diameter 5 cm and throat diameter 1 cm). The other end formed an elliptical cross-section (minor axis length 1 mm, major axis length 15 mm), which was merged with different designed baffles.

In both cases, the whole setup was mounted on a pan-tilt-unit (FLIR Motion Control System PTU-D48E), which provided 180° azimuth and 120° elevation scanning range with a rotation step size of 1° or 3°. Three repeated acoustic measurements were carried out for each prototype conformation to establish repeatability and reduce measurement noise through averaging.

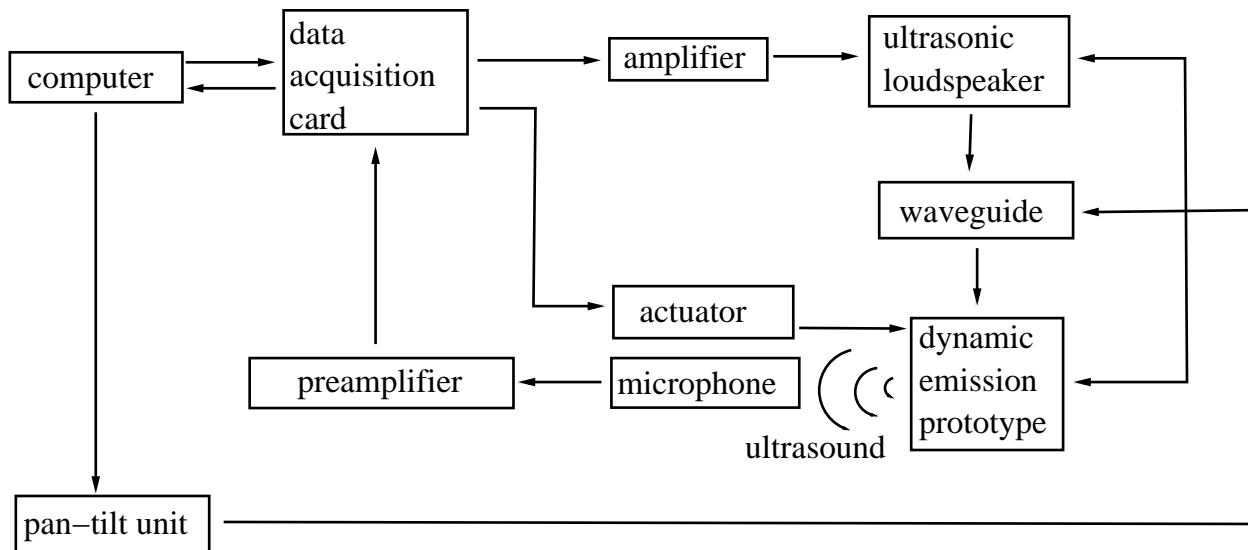


Figure 2.5: Typical components of the acoustic measurements: sound generation and propagation, data acquisition, prototype orientation and actuation.

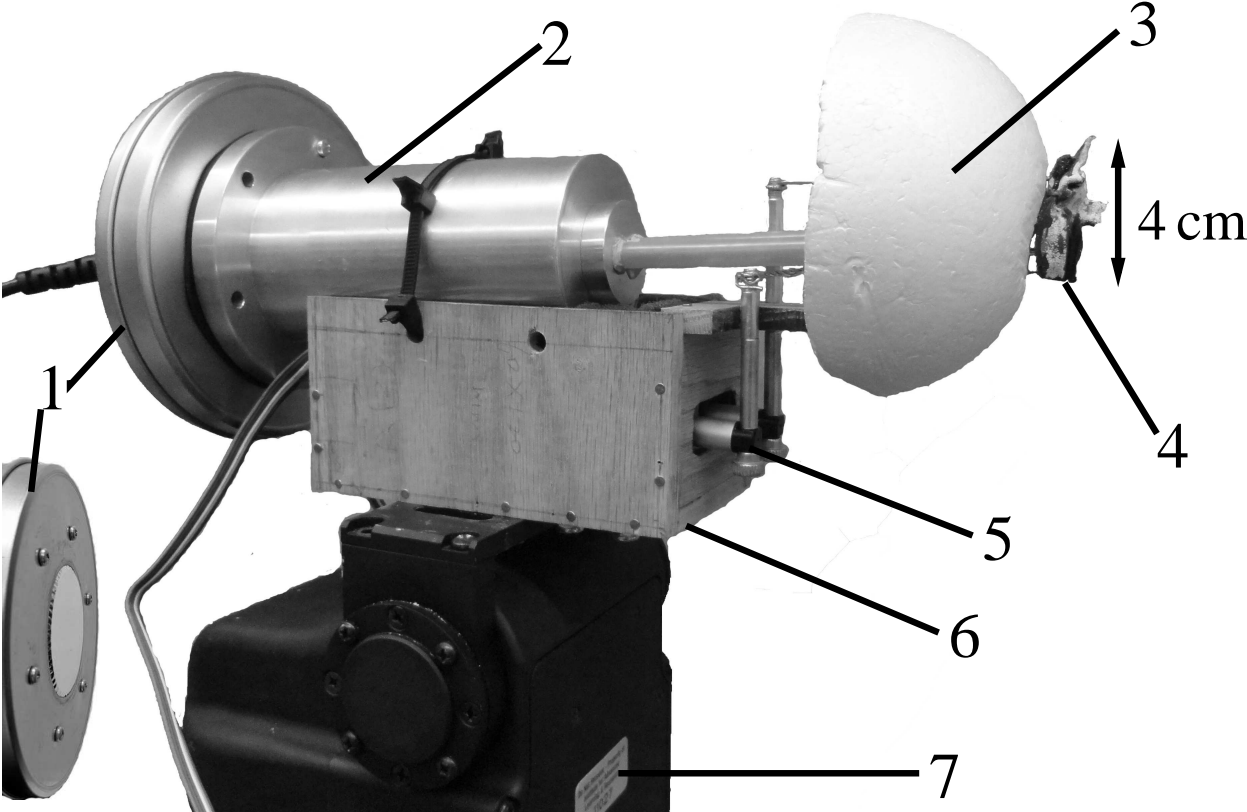


Figure 2.6: Experimental setup for characterization of the dynamic noseleaf: 1) ultrasonic loudspeaker, 2) conical waveguide, 3) Styrofoam, 4) noseleaf (Figure 2.1c), 5) linear actuator, 6) frame, 7) pan-tilt unit.

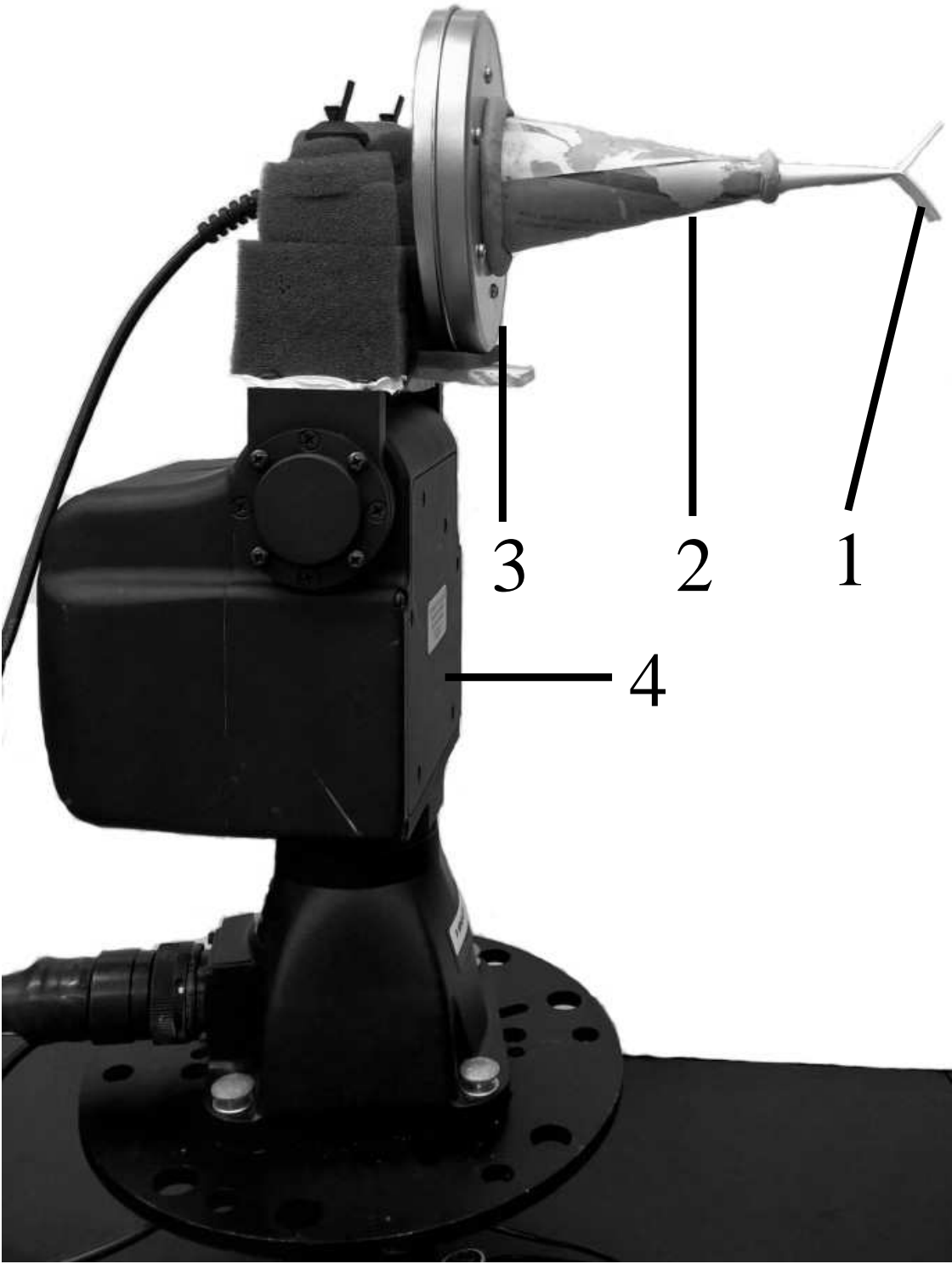


Figure 2.7: Experimental setup for characterization of the dynamic baffles: 1) dynamic baffle (shown here is a straight baffle, Figure 2.4c), 2) conical waveguide, and 3) ultrasonic loudspeaker mounted on a 4) pan-tilt unit.

## 2.7 Signal Processing

Different signal processing approaches were used to characterize the dynamic noseleaf and baffle.

For the dynamic noseleaf experiments, the frequency domain response was obtained by applying a fast Fourier transform with 2048 points to the time domain signals.

For one selected frequency from 30 kHz to 40 kHz, the gains of the one particular frequency over the scanning space ( $-90^{\circ}$ - $90^{\circ}$  azimuth,  $-30^{\circ}$ - $90^{\circ}$  elevation, resolution:  $3^{\circ}$ , linear scale) were used to describe the radiation pattern (2D beampattern) of the different noseleaf configurations (Figure 2.8).

Same technique was used to characterize the static bending effect of the baffles but for 1D beam-pattern (azimuth:  $-90^{\circ}$  to  $90^{\circ}$ , elevation:  $0^{\circ}$ , resolution:  $3^{\circ}$ , dB scale, Figure 2.8d).

Root-mean-square (rms) differences between beam-gains of two different baffle positions were computed to study the baffle bending effect (using amplitudes on a dB-scale).

For dynamic baffle experiments, the envelopes of the time domain signal (duration 250 ms) in different spatial position (elevation:  $-60^{\circ}$ - $+30^{\circ}$ , azimuth:  $0^{\circ}$ , resolution:  $1^{\circ}$ ) were extracted using Hilbert transform to get the time-variant signature (Figure 2.9). Those envelopes were also normalized with the overall maximum in order to see the systematic difference.

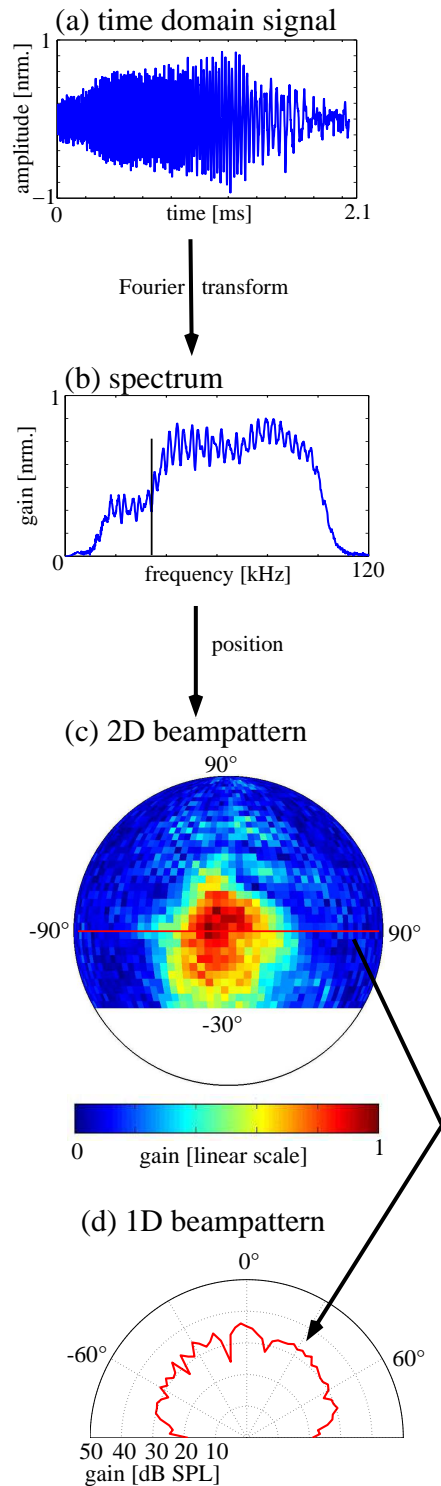


Figure 2.8: Signal processing for radiation pattern: a) acquired time domain signal was transformed into b) frequency domain by using Fourier transform, for one selected frequency (black vertical straight line in (b)) from 30 kHz to 40 kHz, the gain was plotted over full scanning space (azimuth:  $-90^\circ$  to  $90^\circ$ , elevation:  $-30^\circ$  to  $90^\circ$ ) to get the c) 2D beam pattern or just over the horizontal space (azimuth:  $-90^\circ$  to  $90^\circ$ , elevation  $0^\circ$ , red horizontal line in (c)) to get the d) 1D beam pattern.

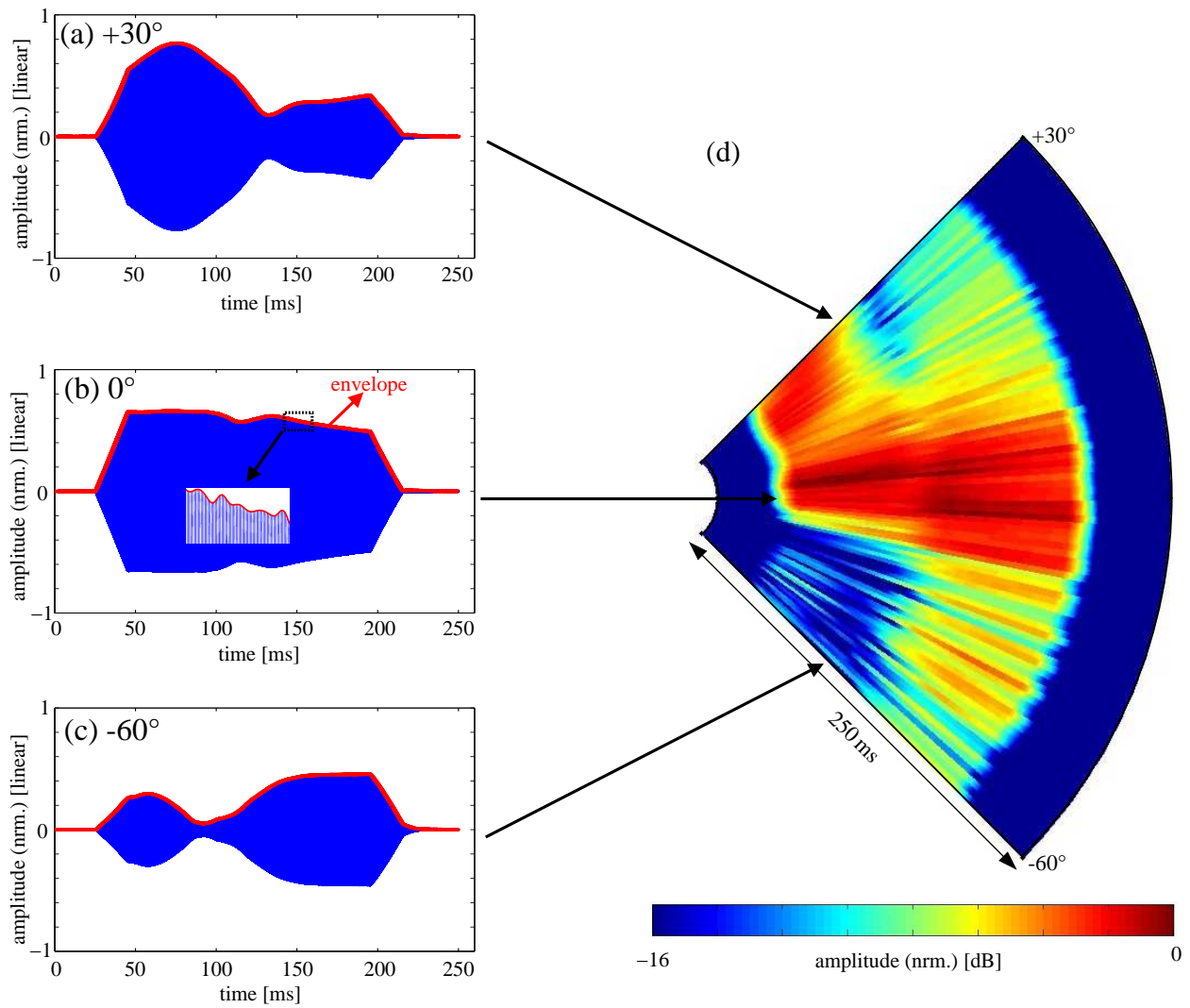


Figure 2.9: Signal processing for the dynamic concave baffle: for one selected frequency from 30 kHz, 40 kHz and 50 kHz, the envelope of time domain data (blue in (a), (b), (c)) was extracted by using Hilbert transform and plotted over position (example: a)  $30^\circ$ , b)  $0^\circ$ , c)  $-60^\circ$ ) to get the d) time variant signature. Inset in (b) shows the detailed envelope pattern.

# Chapter 3

## Results

In the greater horseshoe bat, the sound they emit consists of frequency from 60 -80 kHz. Since the prototype was scaled twice than the original size, so the studied frequency range was from 30 kHz to 40 kHz.

### 3.1 Waveguide Geometry

Overall, the throat diameter had larger effect on the on-axis far-field pressure response than other waveguide parameters (conical horn axial length, tube length).

The increase of the horn axial length and the throat diameter was found to have a increase effect on the average on-axis far-field pressure (Figure 3.1). For 4 cm axial length horn, the average pressure gain was the same (31 dB SPL) in both cases (throat diameter: 3 mm, 7 mm) while for 10 cm axial length horn, the average pressure gain of the 7 mm throat horn was higher (6 dB SPL) than the 3 mm throat horn. Based on those findings, the throat diameter of the horn was fixed to 7 mm.

In the case of horn axial length, tube length and the ratio between them (fixed mouth diameter: 5 cm, throat diameter and tube diameter: 7 mm), all those parameters didn't have big effect on the on-axis far-field pressure amplitude (Figure 3.2, 3.3, 3.4). But the short horn (axial length < 10 cm) had higher peaks and valleys than the rest (Figure 3.2, 3.4).

Although the present of the conical horn and circular tube waveguide did result in a significant drop in the sound pressure level (by about 20 dB), the waveguide still provided reasonable signal-to-noise ratio (around 20 dB).

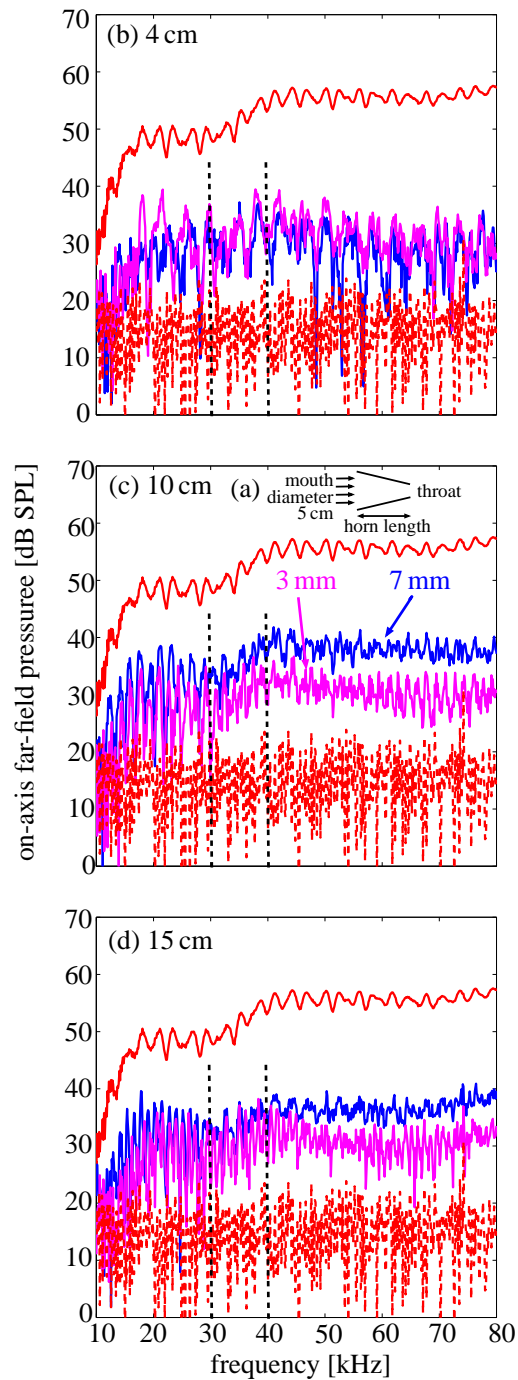


Figure 3.1: Effect of throat diameter for different horn axial lengths on the on-axis far-field pressure: conical horns with the same mouth diameter (5 cm), different throat diameters (blue: 7 mm and magenta: 3 mm) and various horn axial lengths ( b: 4 cm, c: 10 cm, d: 15 cm) were tested. The inset (a) shows the horn cross section and the arrows indicate the sound radiation direction of the loudspeaker. The red solid line and dashed line shows the loudspeaker and noise pressure response respectively. Interested frequency (30 kHz-40 kHz) range was marked by black dashed line.

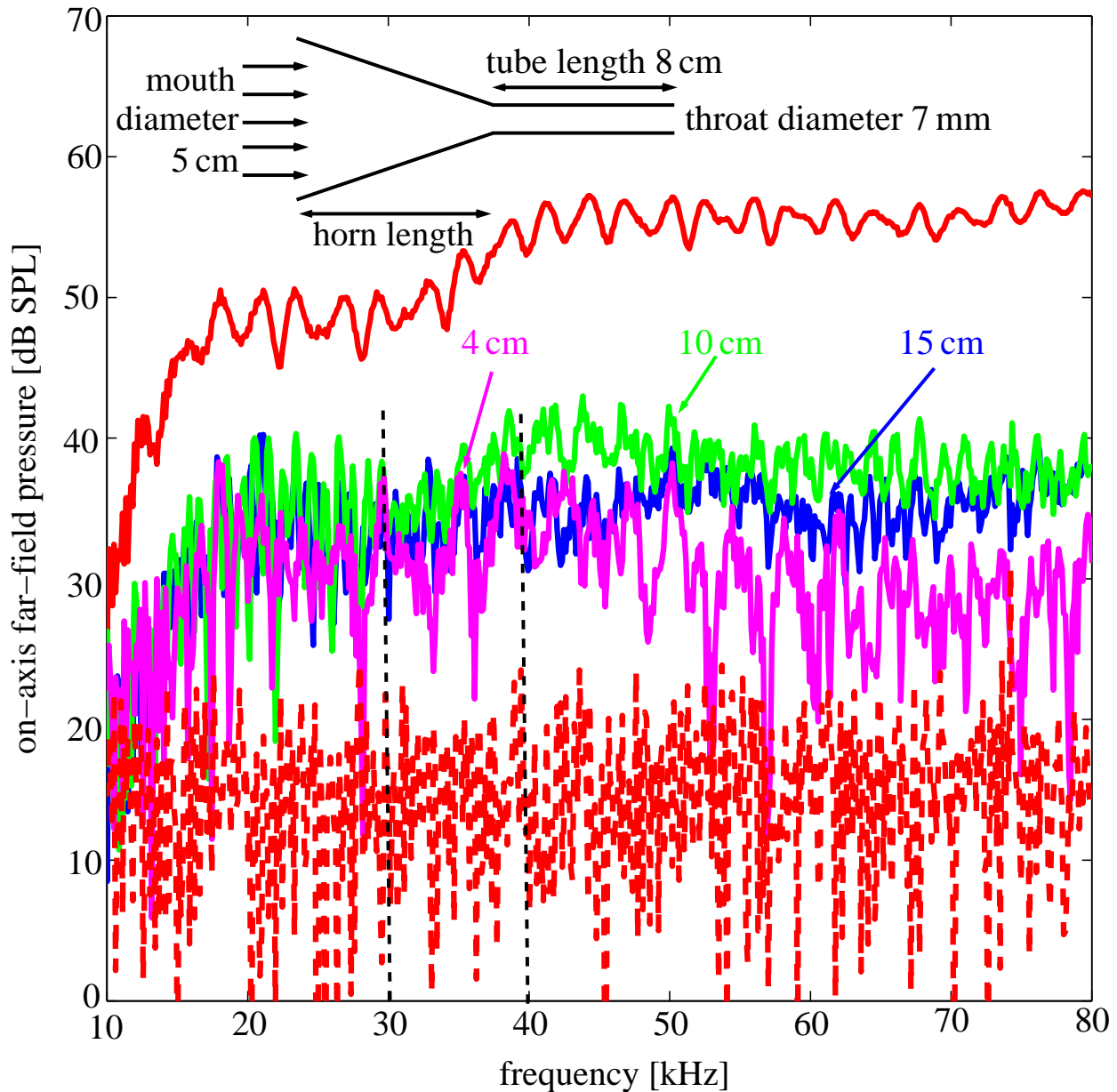


Figure 3.2: Effect of waveguide horn axial length on the on-axis far-field pressure: conical horn and circular tube waveguides with the same mouth diameter (5 cm), throat diameter (7 mm), tube length (8 cm) and different horn axial lengths (magenta: 4 cm, green: 10 cm, blue: 15 cm) were tested. The inset shows the conical horn and circular tube waveguide cross section and the arrows indicate the sound radiation direction of the loudspeaker. Red solid line and dashed line shows the loudspeaker and noise pressure response respectively. Interested frequency range (30 kHz-40 kHz) was marked by black dashed line.

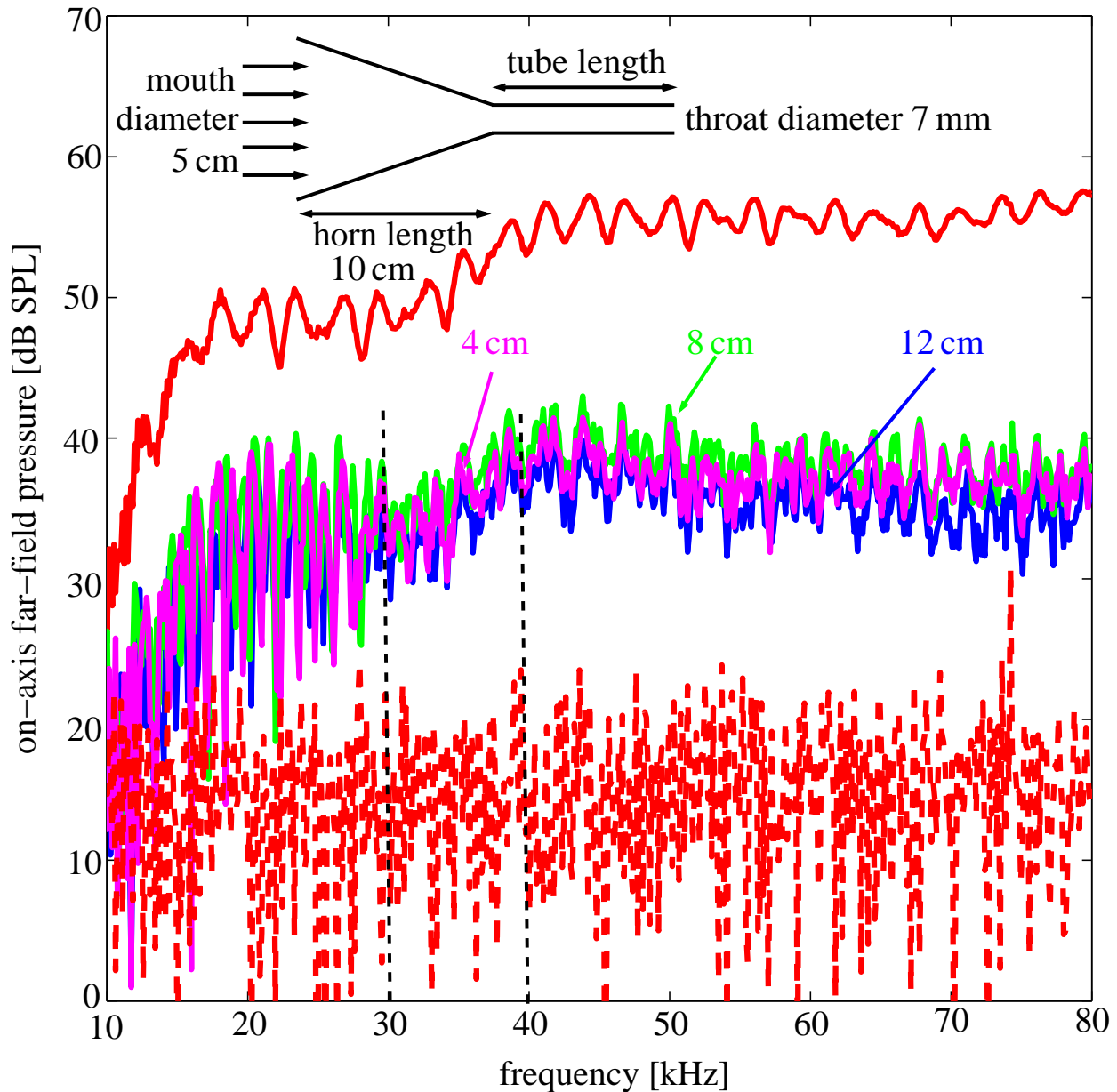


Figure 3.3: Effect of waveguide tube length on the on-axis far-field pressure: conical horn and circular tube waveguides with fixed mouth diameter (5 cm), throat diameter (7 mm), horn axial length (10 cm) and different tube lengths (magenta: 4 cm, green: 8 cm, blue: 12 cm) were tested. The inset shows the conical horn and circular tube waveguide cross section and the arrows indicate the sound radiation direction of the loudspeaker. Red solid line and dashed line shows the loudspeaker and noise pressure response respectively. Interested frequency range (30 kHz-40 kHz) was marked by black dashed line.

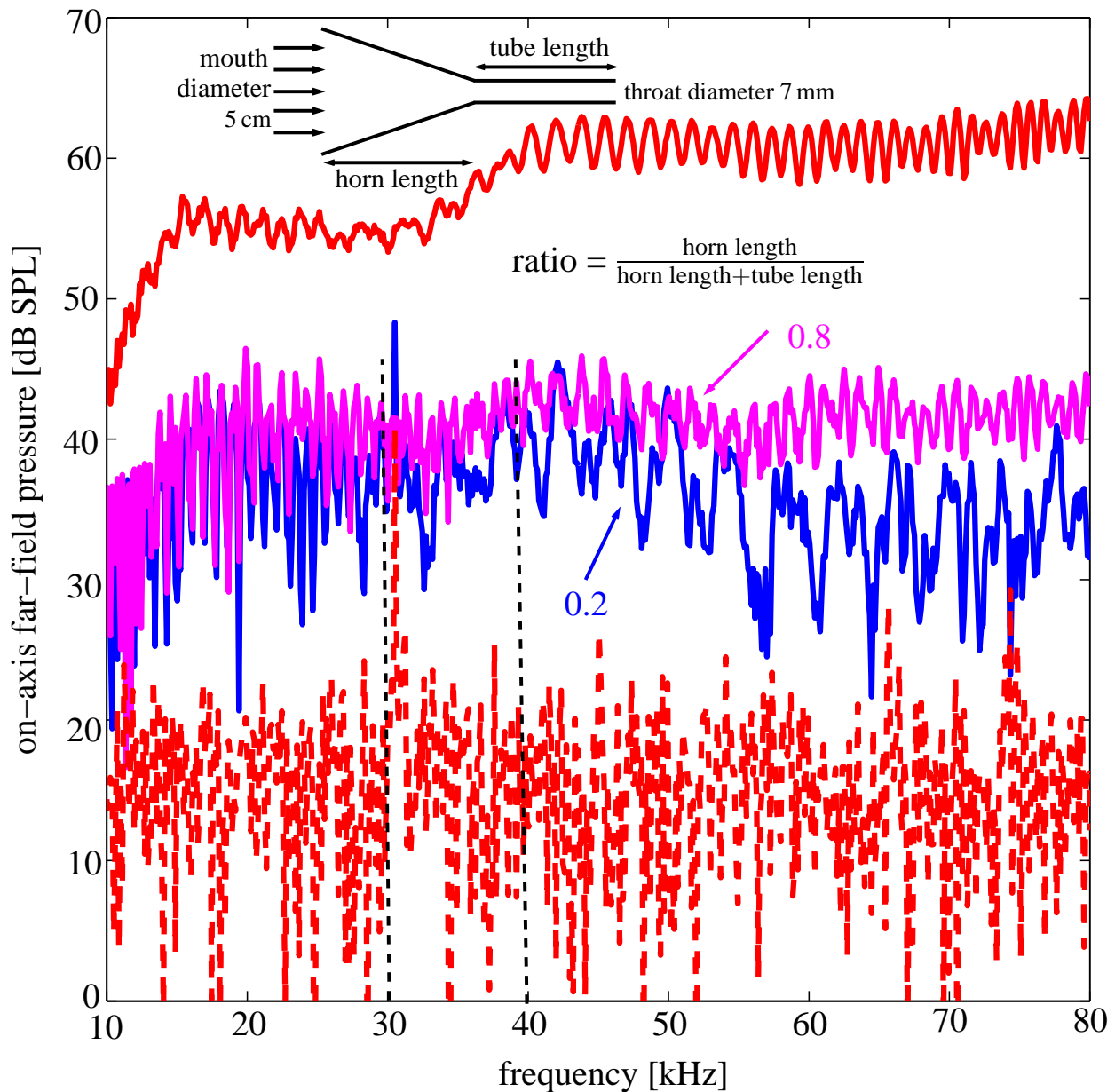


Figure 3.4: Effect of horn axial length and tube length ratio on the on-axis far-field pressure: two different conical horn and circular tube waveguides with the same mouth diameter (5 cm) and throat diameter (7 mm) were tested (blue: horn axial length 4 cm, tube length 16 cm, ratio 0.2; magenta: horn axial length 15 cm, tube length 5 cm, ratio 0.8. Here just shows two examples of Figure 2.2). The top inset shows the conical horn and circular tube waveguide cross section and the arrows indicate the sound radiation direction of the loudspeaker. Red solid line and dashed line shows the loudspeaker and noise pressure response respectively. Interested frequency range (30 kHz-40 kHz) was marked by black dashed line.

## 3.2 Lancet Bending

It was shown that the deformations of the lancet didn't have obvious effect on the beampattern (Figure 3.5) in most of the frequencies. In few frequencies, bending the lancet narrowed the beampattern.

Take 38 kHz of repetition (b) for example, as the lancet was bent from  $0^\circ$  to  $5^\circ$ , the azimuth  $-6$  dB beamwidth kept almost unchanged ( $21^\circ$ ) and elevation  $-6$  dB beamwidth got narrower ( $51^\circ$ - $33^\circ$ ).

Meanwhile, the max beam-gain difference between the upright position and the bending stage of the lancet was around 1 dB over the entire beampattern.

Experiment repetitions of the biomimetic prototype was found to share qualitatively common features (Figure 3.5). All beampatterns were dominated by a mainlobe and as the frequency increased, the lobe narrowed in the azimuth direction.

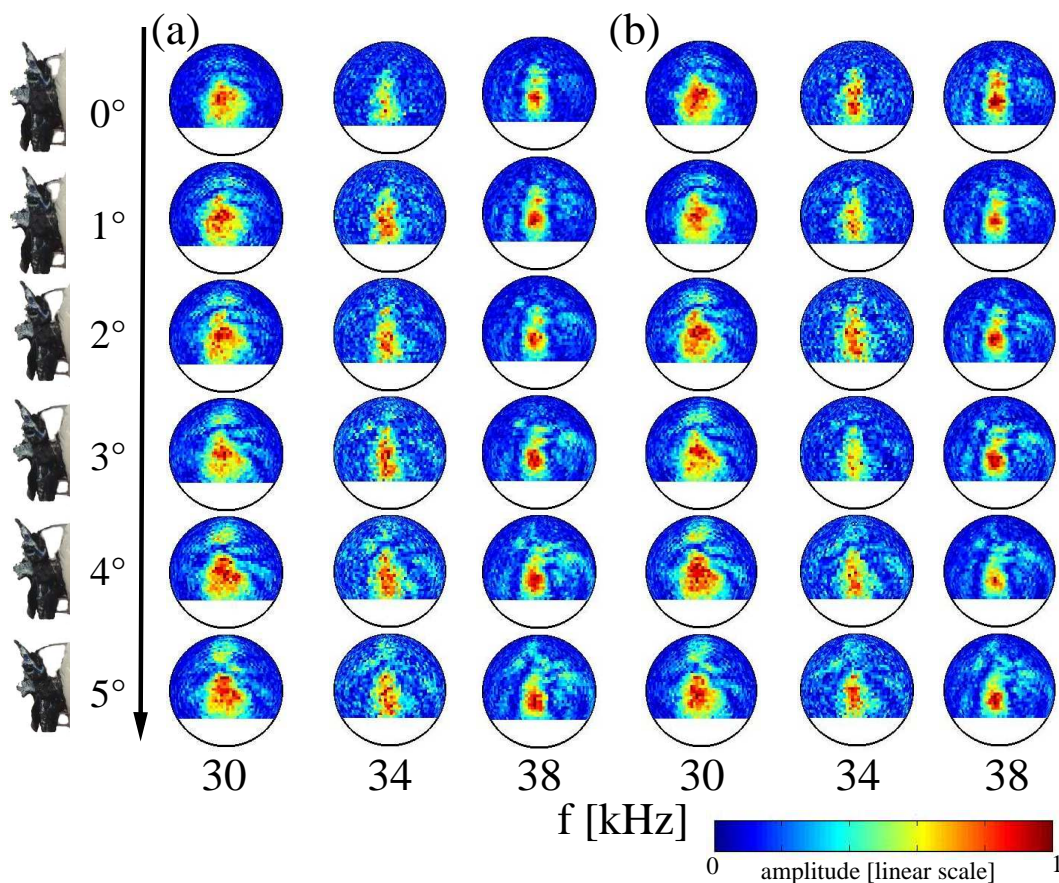


Figure 3.5: Beampatterns at various bending stages of the noseleaf replica: for each experimental repetition (a and b), the lancet was bent from  $0^\circ$  to  $5^\circ$  in steps of  $1^\circ$ , frequencies range from 30 kHz (corresponds to 60 kHz in bats) to 38 kHz (corresponds to 76 kHz in bats) in steps of 4 kHz. Experiment setup was showed in Figure 2.6 and signal processing method was showed in Figure 2.8.

### 3.3 Outlet Geometry

It was observed that the narrow direction of the elliptical outlet produced an omnidirectional beam-pattern compared with the circular outlet.

The diameter of the circular outlet had influences on the pressure gain as well as the beamwidth of the beam-pattern (Figure 3.6). The increase of the circular outlet diameter did result in the increase of the on-axis far-field pressure amplitude (Table 3.1). For all the studied diameter cases (2 mm, 6 mm and 10 mm), the maximum pressure gain difference was 7 dB SPL, 10 dB SPL, 6 dB SPL, 7 dB SPL, 8 dB SPL 7 dB SPL for 30 kHz-40 kHz (2 kHz steps) respectively. On the other hand, the increase of the circular outlet diameter led to a narrower beam-pattern. Take 34 kHz for example, the -6 dB beamwidth was 102°, 72°, 69° for 2 mm, 6 mm and 10 mm circular outlet respectively.

The acoustic effect of the elliptical outlet behaved different than the circular outlet (Figure 3.7). Beam-pattern measured along the minor axis (1 mm) of the elliptical outlet showed almost an isotropic beam-pattern ( $> 120^\circ$ ), the minimum gain change is 4 dB SPL and maximum gain change is 7 dB SPL within  $120^\circ$ . In contrast, beam-pattern measured along the major axis (15 mm) was highly directional (within  $60^\circ$ ). Take 34 kHz for example, the -6 dB beamwidth was  $39^\circ$  for major axis (15 mm) and  $164^\circ$  for minor axis (1 mm).

Beam-pattern measured along the 3 mm minor axis had a similar pattern of the 1 mm minor axis, but had a slightly higher (3 dB) on-axis far-field pressure amplitude. In contrast, on-axis beam-gains of the 15 mm major axis and 1 mm minor axis were the same for all frequencies.

The omnidirectional beam-pattern is the one we want since if we attached a baffle around it, the beam-pattern can be easily changed and any change in the beam-pattern is due to the baffle effect.

In the following, the results shown were measured along the minor axis (1 mm) of the elliptical outlet.

Table 3.1: Influence of the circular outlet diameter on the on-axis far-field pressure (dB SPL) for different frequencies

diameter (mm)	30 kHz	32 kHz	34 kHz	36 kHz	38 kHz	40 kHz
2	34	31	34	35	37	38
6	39	38	38	40	41	44
10	41	41	40	42	45	45

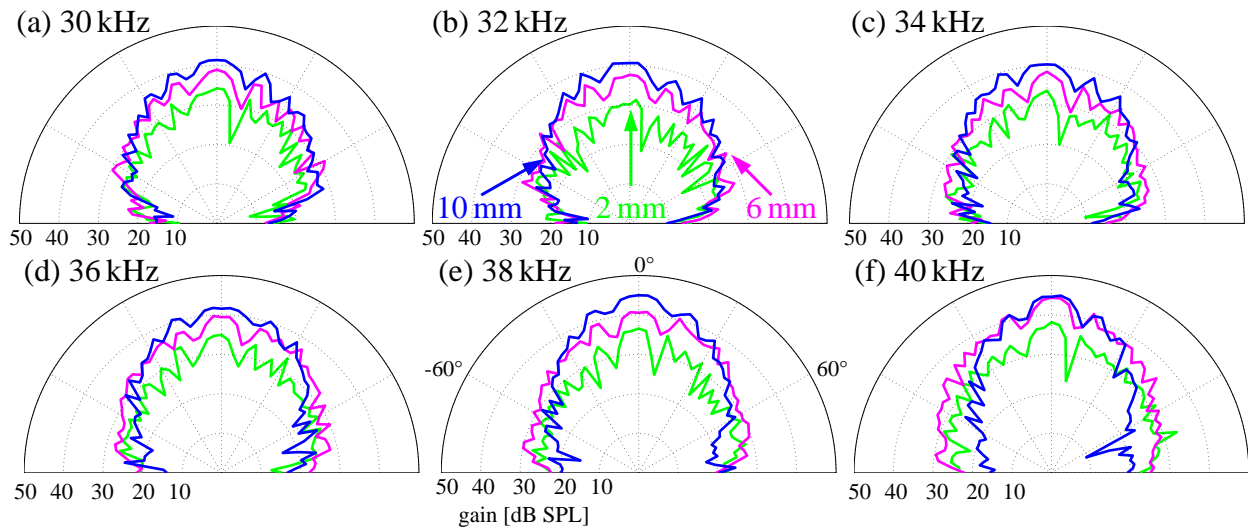


Figure 3.6: Influence of circular outlet diameter on the beampatterns: a) 30 kHz, b) 32 kHz, c) 34 kHz, d) 36 kHz e) 38 kHz, f) 40 kHz. Circular outlets with different diameters (green: 2 mm, magenta: 6 mm, blue: 10 mm) were tested. Signal processing method was showed in Figure 2.8.

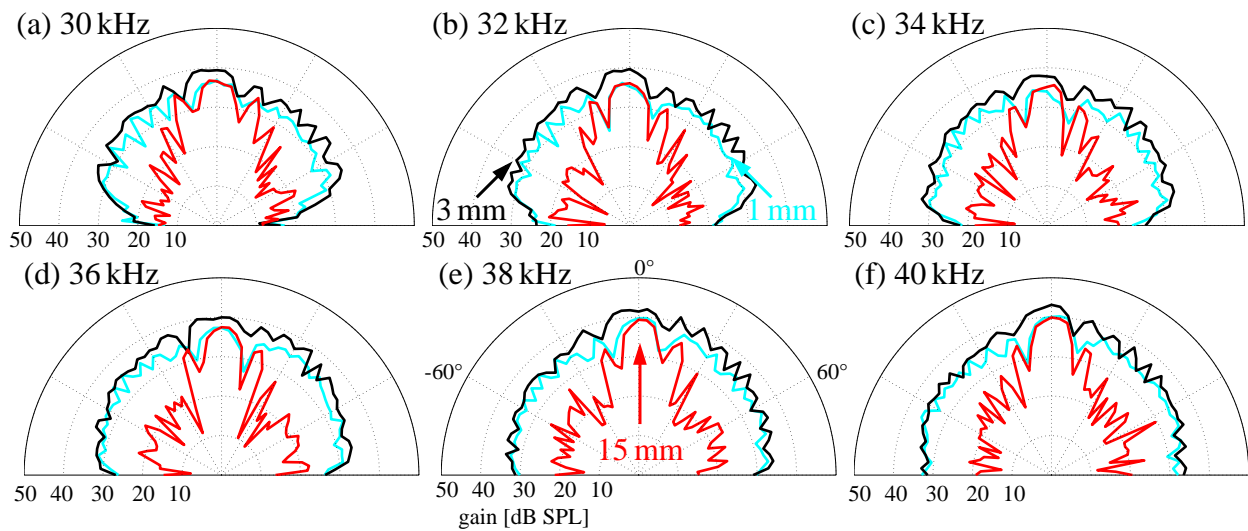


Figure 3.7: Influence of elliptical outlet on the beampatterns: a) 30 kHz, b) 32 kHz, c) 34 kHz, d) 36 kHz e) 38 kHz, f) 40 kHz. Elliptical outlets with the same major axis (red: 15 mm) and different minor axes (black: 3 mm, cyan: 1 mm) were tested. Signal processing method was showed in Figure 2.8.

### 3.4 Baffle Geometry

For the same amount of static baffle angle change, the 2 cm baffle had a narrower beam pattern and higher on-axis far-field pressure gain change than the 1 cm baffle.

In terms of the 1 cm baffle, as the baffle semiangle was changed from  $60^\circ$  to  $30^\circ$ , the beam pattern remained almost constant in low frequency and got narrower in high frequency (Figure 3.8, Table 3.2). The maximum -6 dB beamwidth change was  $35^\circ$  for 38 kHz and on-axis far-field pressure amplitude remained almost constant (maximum difference was 1 dB SPL for all frequencies, Table 3.3).

In terms of 2 cm baffle, as the baffle semiangle was changed from  $60^\circ$  to  $30^\circ$ , the beam pattern got narrower for all frequencies (Figure 3.8, Table 3.2). The maximum -6 dB beamwidth change was  $42^\circ$  for 38 kHz and on-axis far-field pressure value increased for every frequency (maximum difference was 4 dB SPL for 38 kHz, Table 3.3).

In summary, the 2 cm baffle produced more beam pattern change than the 1 mm in terms of beamwidth and amplitude.

Table 3.2: Influence of the baffle dimension on the -6 dB beamwidth ( $^\circ$ ) for different frequencies (beam pattern was measured along the minor axis of the elliptical outlet)

baffle length (cm)	baffle angle ( $^\circ$ )	30 kHz	34 kHz	38 kHz
1	30	53	50	40
1	60	59	71	85
2	30	37	28	28
2	60	58	54	70

Table 3.3: Influence of the baffle dimension on the on-axis far-field pressure (dB SPL) for different frequencies (beam pattern was measured along the minor axis of the elliptical outlet)

baffle length (cm)	baffle angle ( $^\circ$ )	30 kHz	34 kHz	38 kHz
1	30	36	35	39
1	60	35	34	38
2	30	40	39	40
2	60	38	36	36

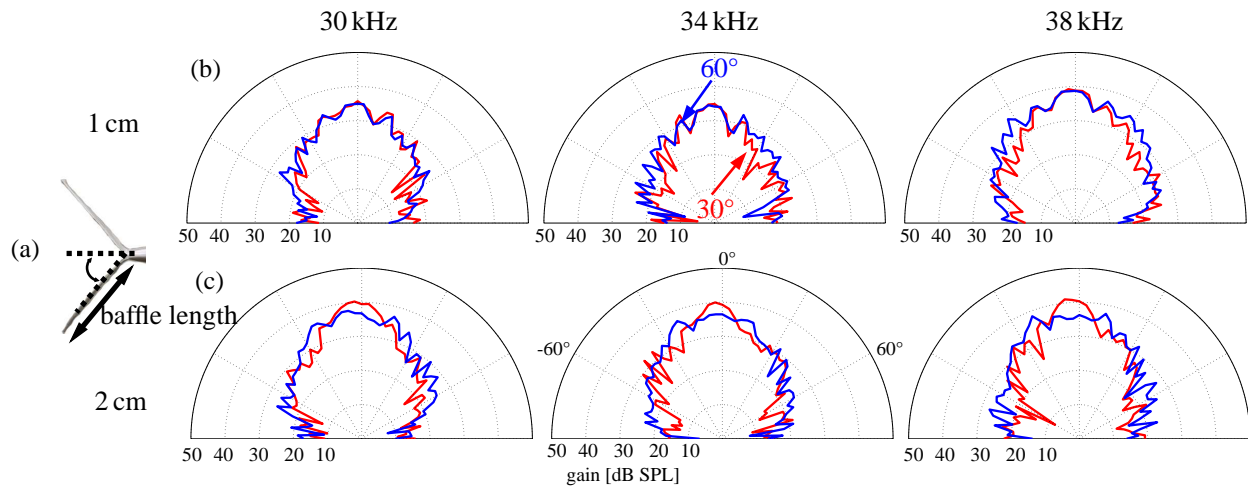


Figure 3.8: Beampattern effects due to the length of the straight baffle: different baffle lengths (b, 1 cm; c, 2 cm) and different baffle semiangles (blue: 60°, red: 30°) were tested at various frequencies: 30 kHz, 34 kHz, 38 kHz. The dashed lines indicate the semiangle of the baffle opening (inset a, shown here is a semiangle of 60°). Experiment setup was showed in Figure 2.7, beampattern was measured along the minor axis (1 mm) of the elliptical outlet. Signal processing method was showed in Figure 2.8.

### 3.5 Static Characterization of Straight Baffle

The median of the rms-difference depended on the bending angle of the straight baffle linearly.

The median rms-difference between repeated measurements of the beampatterns associated with the 90°-open angle was found to be 2.8 dB (Figure 3.9, 0°), which was regarded as the system noise level for the all tested cases.

Over the angular bending distance of 60°, the rms difference between the beampattern gains increased monotonically from a base (measurement noise) level 2.8 dB to 6 dB, this relationship was found to be approximately linear (linear regression for median rms difference versus angular difference:  $r^2=0.97$ , regression slope: 0.05 dB/°) (Figure 3.9, Table 3.4).

The increasing on-axis pressure and narrowing beamwidth effect associated with the rotation of the flanges accounts for the increasing rms-difference. Take 34 kHz for example (Figure 3.9(c)), as the flap was rotated, the on-axis pressure gain was changed from 32 dB SPL to 39 dB SPL (Table 3.5) and the -6 dB beamwidth was changed from 119° to 30° corresponding to baffle opening angle 90° and 30° respectively (Table 3.6).

Table 3.4: Influence of the bending angle on the median root mean square difference for 2 cm straight baffle

bending angle (°)	median [minimum, maximum] rms-difference (dB)
0	2.8 [2.3, 3.3]
10	3.0 [2.4, 3.7]
20	3.5 [2.9, 4.6]
30	3.9 [3.4, 4.5]
40	4.4 [3.7, 6.2]
50	5.2 [3.9, 6.5]
60	6.0 [4.5, 8.2]

Table 3.5: Influence of the bending angle on the on-axis far-field pressure response of 34 kHz for 2 cm straight baffle

bending angle (°)	on-axis far-field pressure response of 34 kHz (dB)
30	39
40	37
50	35
60	33
70	34
80	33
90	32

Table 3.6: Influence of the bending angle on the -6 dB beamwidth of 34 kHz for 2 cm straight baffle

bending angle (°)	-6 dB beamwidth of 34 kHz (°)
30	30
40	51
50	69
60	84
70	100
80	101
90	119

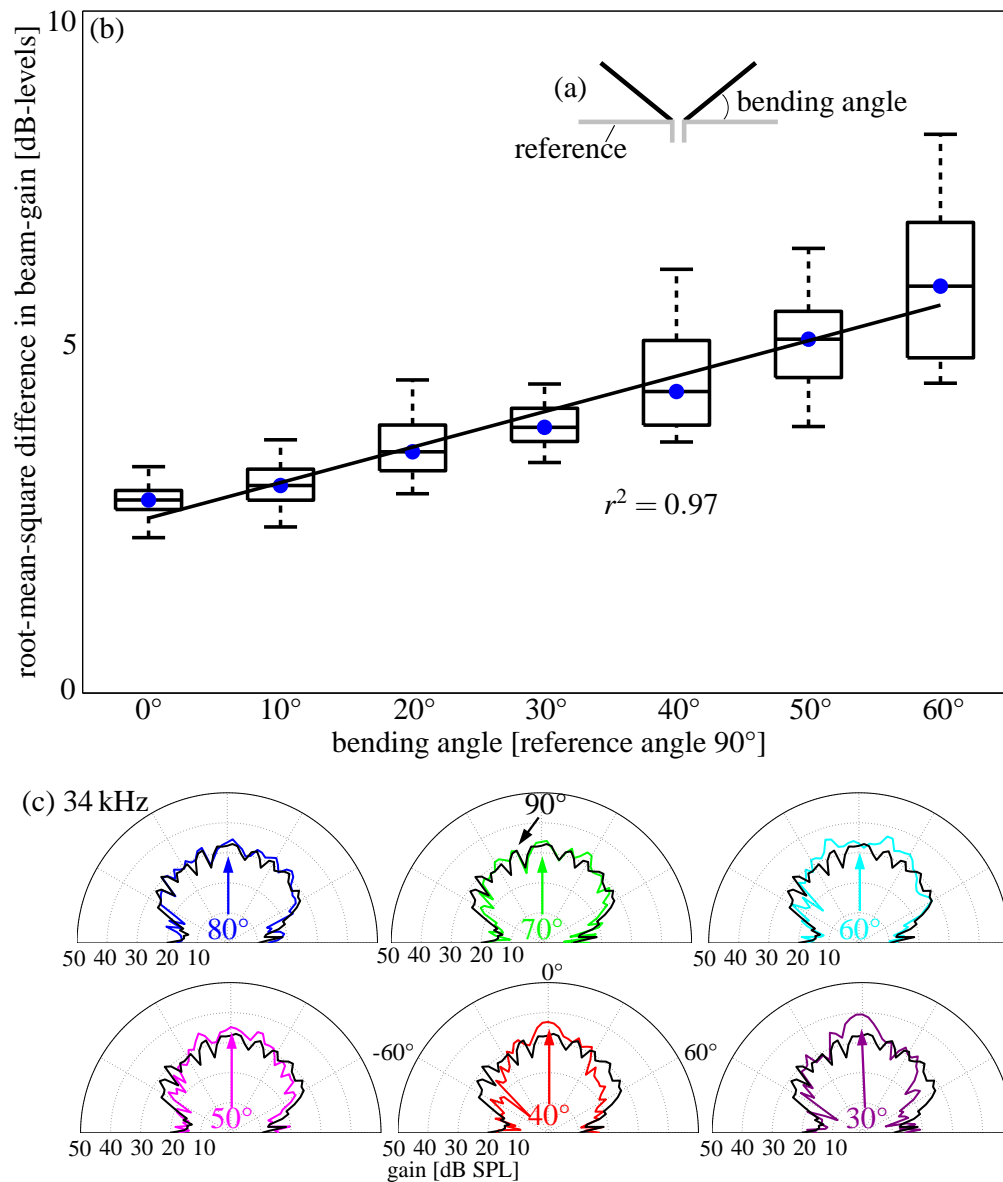


Figure 3.9: Beampattern effects due to static bending of the straight baffle: a) reference opening angle was 90° and bending angle varied, b) root-mean-square gain difference between beampatterns produced by a 90°-reference and a tested opening angle, all rms differences were computed with averaging over 21 frequencies ranging from 30 kHz to 40 kHz in steps of 0.5 kHz as well as over angle, black straight line shows the linear regression between the bending angle and the median (blue dot) of the rms difference, slope 0.05 dB/°, coefficient of determination  $r^2 = 0.97$ , c) example beampatterns shown are for a frequency of 34 kHz of different baffle opening angles: 90°(black), 80°(blue), 70°(green), 60°(cyan), 50°(magenta), 40°(red), 30°(purple). In the box-and-whisker plots, the whiskers denote the location of the minimum and maximum, the edges of the box the first and third quartiles, and the horizontal line the median. Experiment setup was showed in Figure 2.7, beampattern was measured along the minor axis (1 mm) of the elliptical outlet. Signal processing method was showed in Figure 2.8.

### 3.6 Static Characterization of Concave Baffle

The beampatterns associated with the bending concave baffle behaved very different from the straight baffle flaps.

From an rms-error base line of 2.8 dB (identical to straight baffle), the rms difference between beampatterns jumped to 5.7 dB within just a bending of 10° (Figure 3.10). For larger bending angles, the rms difference appeared to oscillate between values as low as 4 dB (median value for 30°, Figure 3.10) and as high as 5.8 dB (median value for 40°, Figure 3.10).

The oscillations of the rms-difference were due to the pronounced sidelobes in the beampatterns that were associated with the concave baffle (Figure 3.10a-f). As the baffle was bent, the location of the sidelobes and the notches that separated them from the mainlobe were shifted, when the directions of sidelobes and notches coincided, a large rms-difference resulted. Whenever the lobes of the compared beampattern overlapped, the rms-difference was small.

Small-scale rotations (0° to 10° in steps of 2° or 3°) showed that the transitions between similar and dissimilar beampatterns within the bending were smooth as well (Figure 3.11). The distinguish difference was that the sidelobe in the beampatterns changed its angular position as well as gain. Again, the relationship between rms differences and bending angle was approximately linear ( $r^2=0.87$ , i.e., not quite as well linearly correlated as the straight baffle, Figure 3.11), but this happened over a much smaller angular range of 10° (regression slope 0.2 dB/°, 4× the slope for the straight baffle, Figure 3.10, Table 3.7). More importantly, to get the same rms-difference, the straight baffle need to rotate 6× (60°) larger than the concave baffle.

Table 3.7: Influence of the bending angle on the median root mean square difference for 2 cm concave baffle

bending angle (°)	median [minimum, maximum] rms-difference (dB)
0	2.8 [2.3, 3.3]
10	5.7 [4.8, 6.5]
20	5.0 [3.9, 5.5]
30	4.0 [3.3, 5.7]
40	5.8 [4.8, 6.9]
50	5.5 [4.5, 6.6]
60	4.4 [3.5, 5.1]

Table 3.8: Influence of the small bending angle on the median root mean square difference for 2 cm concave baffle

bending angle (°)	median [minimum, maximum] rms-difference (dB)
0	2.8 [2.3, 3.3]
3	4.4 [3.8, 5.2]
5	4.4 [3.3, 5.2]
7	5.0 [4.0, 5.8]
10	5.7 [4.8, 6.5]

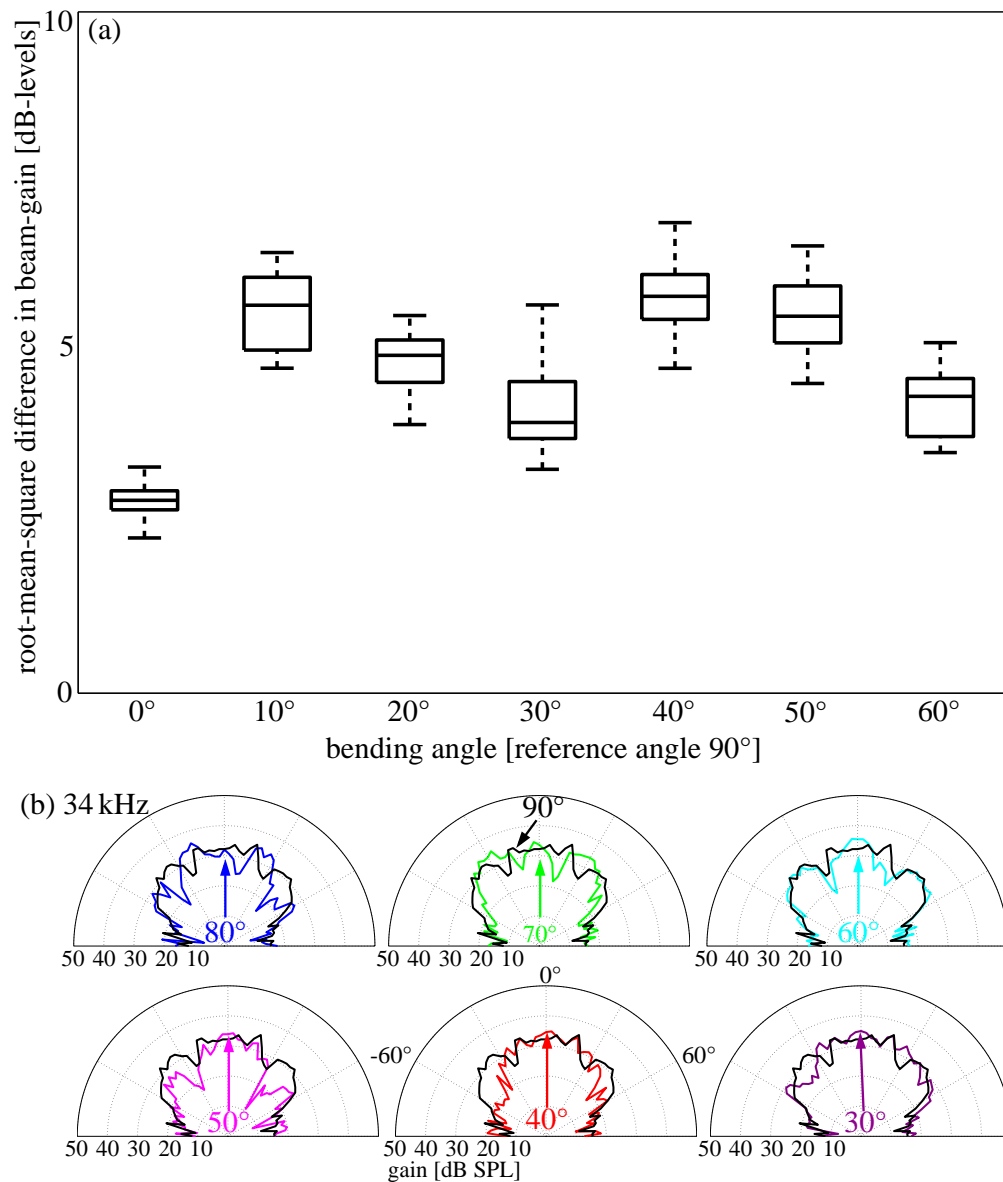


Figure 3.10: Beampattern effects due to static bending of the concave baffle: a) root-mean-square gain difference between beampatterns produced by a 90°-reference and a tested opening angle (Figure 3.9a), all rms differences were computed with averaging over 21 frequencies ranging from 30 kHz to 40 kHz in steps of 0.5 kHz as well as over angle, b) example beampatterns shown are for a frequency of 34 kHz of different baffle opening angles: 90° (black), 80° (blue), 70° (green), 60° (cyan), 50° (magenta), 40° (red), 30° (purple). In the box-and-whisker plots, the whiskers denote the location of the minimum and maximum, the edges of the box the first and third quartiles, and the horizontal line the median. Experiment setup was showed in Figure 2.7, beampattern was measured along the minor axis (1 mm) of the elliptical outlet. Signal processing method was showed in Figure 2.8.

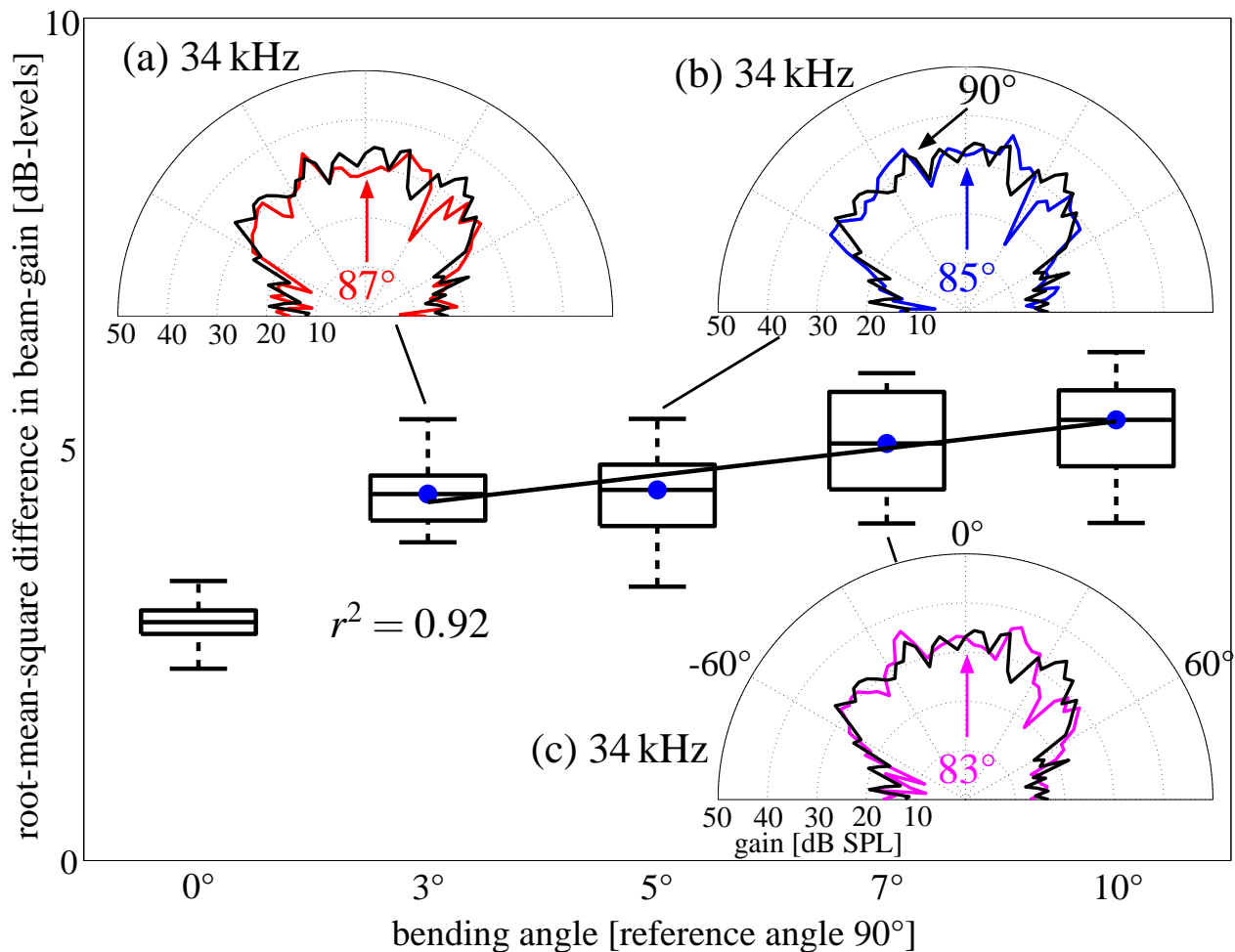


Figure 3.11: Beam pattern effects due to static bending of the concave baffle over small angles ( $0^\circ$  to  $10^\circ$ ). Root-mean-square gain difference between beam patterns produced by a  $90^\circ$ -reference and a tested opening angle (Figure 3.9a). The reference opening angle was  $90^\circ$  for all conditions (Figure 3.9a). Black straight line shows the linear regression between the bending angle (from  $3^\circ$  to  $10^\circ$ ) and the median (blue dot) of the rms difference, slope  $0.2 \text{ dB}^\circ$ , coefficient of determination  $r^2 = 0.92$ . The example beam pattern plots show beam patterns for inwards bending angles relative to the reference of (a)  $3^\circ$ , (b)  $5^\circ$ , and (c)  $7^\circ$ . All other experimental and display parameters were the same as Figure 3.10. Experiment setup was showed in Figure 2.7, beam pattern was measured along the minor axis (1 mm) of the elliptical outlet. Signal processing method was showed in Figure 2.8.

### 3.7 Dynamic Characterization of Concave Baffle

When the concave baffle was continuously actuated in synchrony with the emission, a signature was created that depended on time, frequency (30, 40, 50 kHz) as well as direction (Figure 3.12).

Take 40 kHz for example (Figure 3.12c,f), when the baffle was held its position, the amplitude of the time domain signal was constant along the time axis and varied across spatial direction. But when the baffle was moved during the pulse, the amplitude of the time domain signal varied both in the time axis and across direction. Moreover, the magnitudes of the lower range ( $-60^\circ$  to  $-30^\circ$ ) of dynamic case was higher than (more than 10 dB difference ) the same range of the static case.

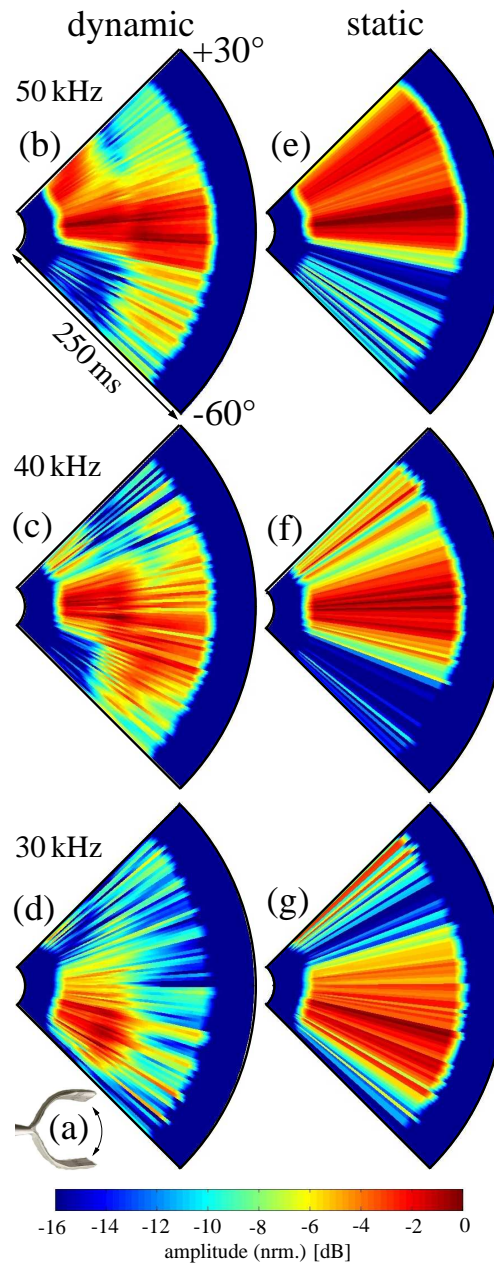


Figure 3.12: Example of a continuous time-variant signature created by motion of a concave baffle: a) measurement direction relative to the baffle, b,c,d) magnitudes (envelope of the analytic signal) of signal received from the dynamic baffle for frequencies of b) 50 kHz, c) 40 kHz, and d) 30 kHz. The static reference (opening angle  $60^\circ$ ) are shown in e) 50 kHz, f) 40 kHz, and g) 30 kHz. The baffle motion executed in this example ranged from  $-60^\circ$  to  $30^\circ$  in 250 ms. Signal was measured along the minor axis (1 mm) of the elliptical outlet. Signal processing method was showed in Figure 2.9.

# Chapter 4

## Discussions

### 4.1 Interpretation of Results

The waveguide dimension, i.e. the horn throat diameter, the horn axial length, plays an important role in the acoustic performance of the waveguide.

The horn throat diameter controls the on-axis far-field pressure response gain. For constant sound intensity inside the horn, the larger the throat area (the larger the throat diameter), the more power it radiates according to sound power equals sound intensity times the area relationship. Hence, the higher on-axis far-field pressure gain for larger throat diameter.

The horn axial length mainly influences the on-axis far-field pressure response pattern. For short horn, the sound reflects more inside the horn than the long horn, thus less sound radiates from the horn, which explains why shorter horn had high peaks and valleys than the longer horn.

The geometry of the outlet, i.e. shape and dimension, determines the on-axis far-field pressure response as well as far-field radiation pattern.

Again, larger outlet area resulted in a higher on-axis far-field pressure output. Meanwhile, the far-field radiation pattern of the circular and elliptical outlet was governed by the following normalized (with respect to the on-axis pressure amplitude) directivity function [101, 102]:

$$D(\theta, \phi) = \frac{2J_1(k \sin \theta \sqrt{b^2 \cos^2 \phi + a^2 \sin^2 \phi})}{k \sin \theta \sqrt{b^2 \cos^2 \phi + a^2 \sin^2 \phi}}$$

where  $a$  is the semi-minor axis and  $b$  is the semi-major axis of the elliptical outlet, when  $a = b$ , the equation reduces to the circular outlet case.  $J_1$  is the first kind Bessel equation.  $\theta$  is the cone angle (determines the beam direction measured with reference to the normal to the outlet plane) and  $\phi$  is the azimuthal angle within the elliptical outlet plane (Figure 4.1a). When  $k \sqrt{b^2 \cos^2 \phi + a^2 \sin^2 \phi}$  is smaller than 1, the far-field radiation pattern is omnidirectional and when it is larger than 1, radiation pattern becomes narrow. Take an elliptical outlet (minor axis 1 mm, major axis 15 mm)

for example, 34 kHz beampattern measured along the minor axis ( $k\sqrt{b^2\cos^2\phi + a^2\sin^2\phi} = 0.3$ ) was more wider than beampattern measured along the major axis ( $k\sqrt{b^2\cos^2\phi + a^2\sin^2\phi} = 5$ ) (Figure 4.1b), which is qualitatively agree with the experimental results.

Since the elliptical outlet produced an omnidirectional beampattern along the minor axis, if one attached baffles perpendicular to the minor axis direction, the beampattern could be easily changed and any change in the beampattern was due to the baffle change, which was showed in the experimental results.

When either straight baffle or concave baffle was attached to the elliptical outlet and if the attached angle was changed, the corresponding acoustic impedance was also changed. Acoustic impedance is a measurement of the sound radiation efficiency. It consists of two parts: real part is acoustic resistance and imaginary part is acoustic reactance. As the baffle opening angle decreases (bending angle increases), the throat acoustic resistance increases [103, 104]. Simulation results by using modal propagation method [105, 106, 107] also showed this kind of trend (Figure 4.2). For a constant velocity source, the acoustic power is proportional to the acoustic resistance [103, 108], thus high acoustic resistance results in high radiation efficiency. Hence the root-mean-square(rms) gain difference between reference angle ( $90^\circ$ ) beampattern and tested angle ( $30^\circ$ - $80^\circ$  in steps of  $10^\circ$ ) beampattern increases as the bending angle increases (Figure 4.3).

On the contrary, the resonance effect of the concave baffle complicates this relationship [109, 110], thus the trend between the rms gain difference and the bending angle of the concave baffle becomes oscillated and continuously moving the concave baffle could have a dramatic time-variant effect.

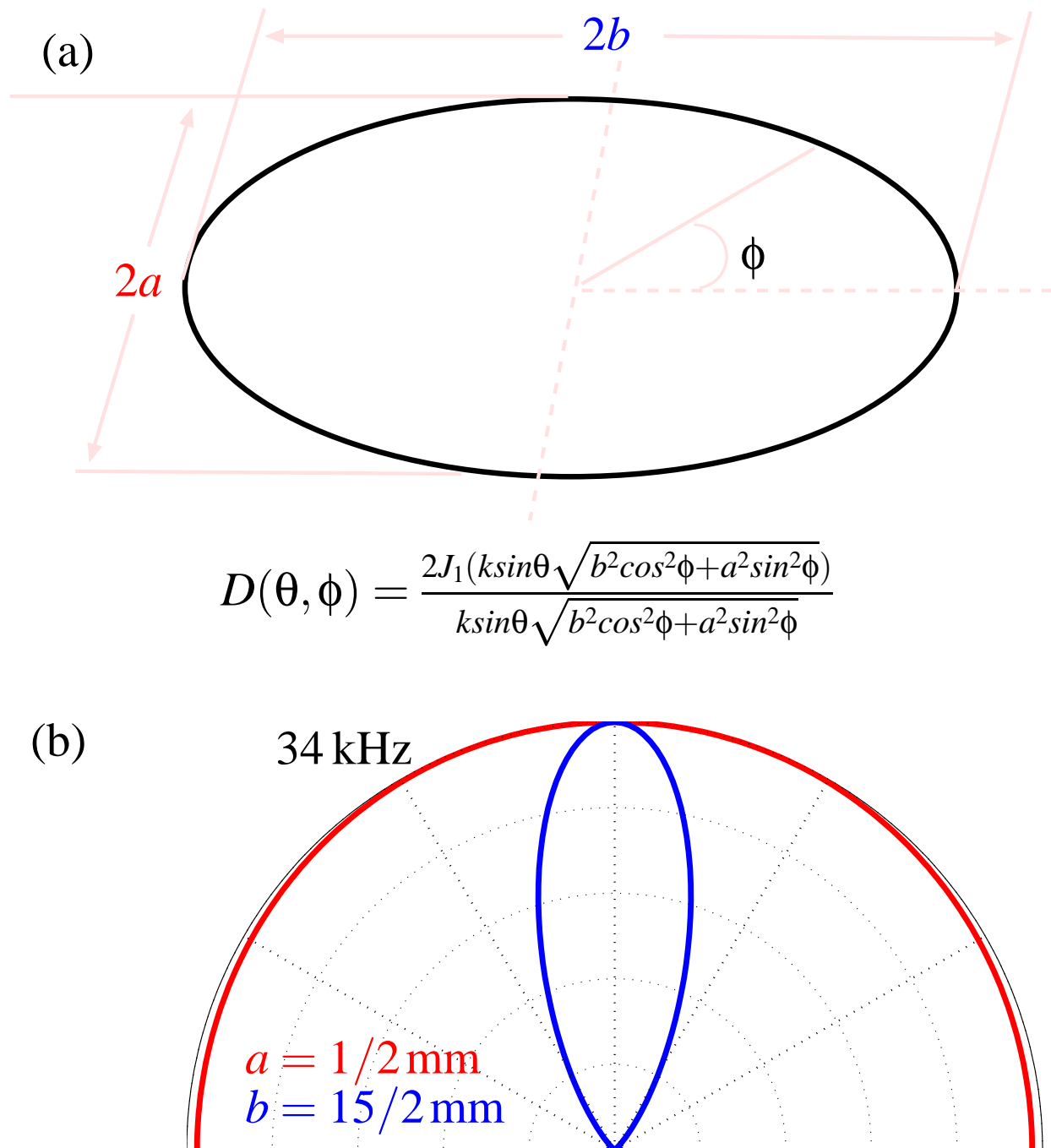


Figure 4.1: Governing equation and examples of the far-field radiation pattern of the elliptical outlet: a) governing equation of the elliptical outlet far-field radiation pattern,  $a$  is the semi-minor axis and  $b$  is the semi-major axis of the elliptical outlet,  $J_1$  is the first kind Bessel equation.  $\theta$  is the cone angle and  $\phi$  is the azimuthal angle within the elliptical outlet plane, b) elliptical outlet far-field radiation pattern of 34 kHz, minor axis length 1 mm (red), major axis length 15 mm (blue).

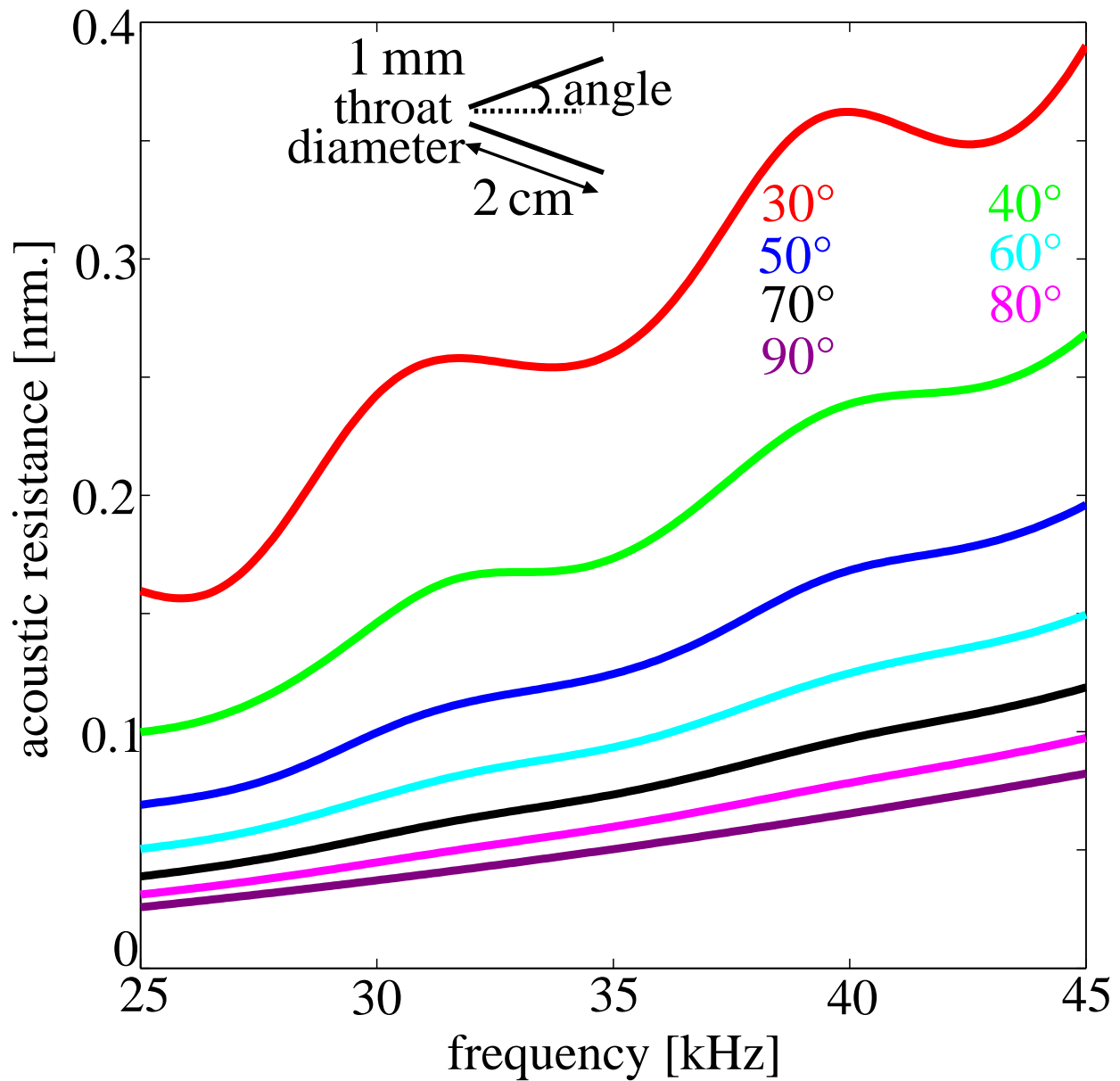


Figure 4.2: Normalized acoustic resistance of conical horn with different horn angles: 30° (red), 40°(green), 50° (blue), 60° (cyan), 70° (black), 80° (magenta), 90° (purple). Inset shows the cross-section of the conical horn, throat diameter 1 mm, horn length 2 cm.

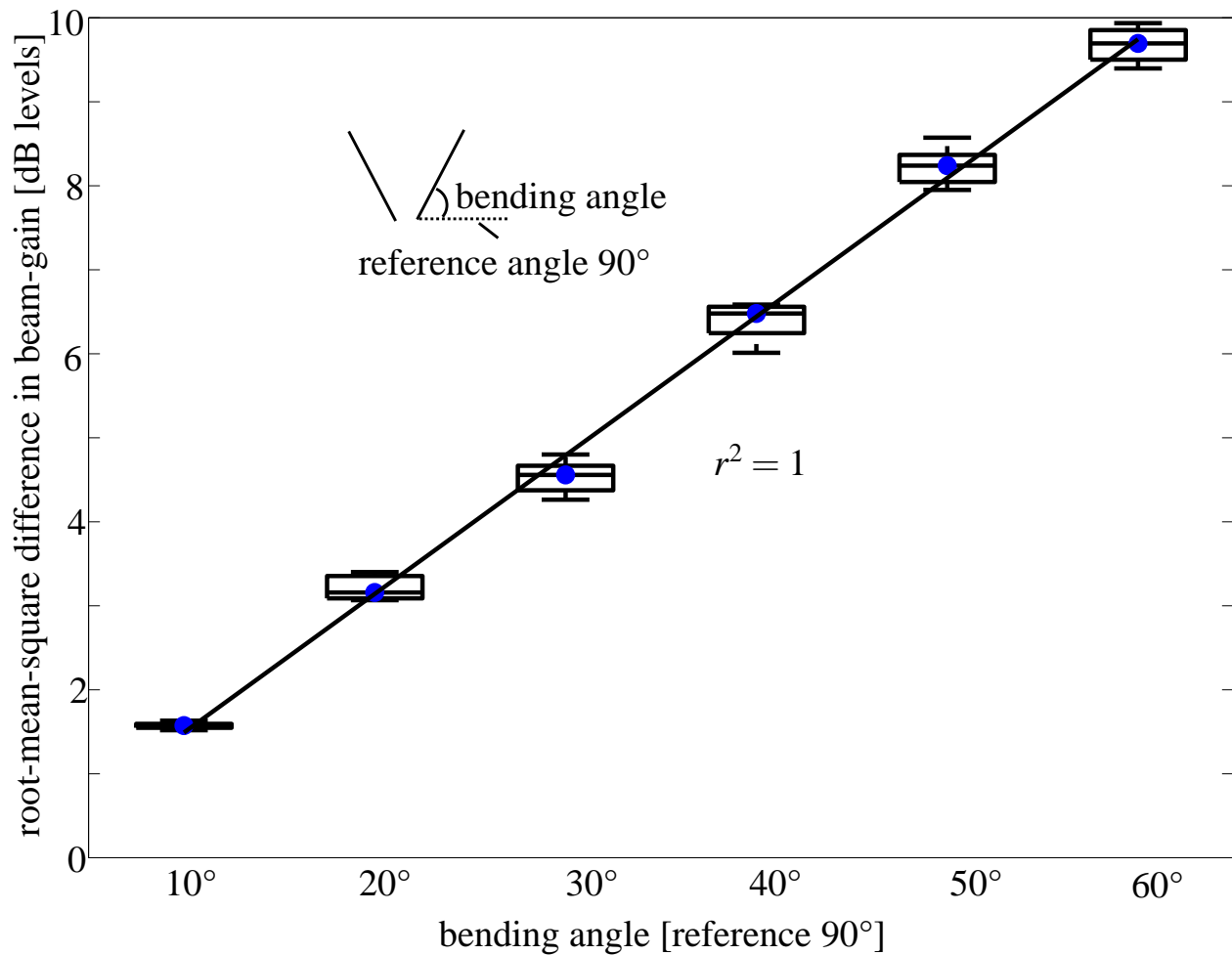


Figure 4.3: Bending effect of the conical horn angle on the root-mean-square (rms) gain difference between reference angle ( $90^\circ$ ) beampattern and tested angle ( $30^\circ$ - $80^\circ$  in steps of  $10^\circ$ ) beampattern: black straight line shows the linear regression between the bending angle and the median (blue dot) of the rms difference, slope  $0.2 \text{ dB}/^\circ$ , coefficient of determination  $r^2 = 1$ . RMS beam-gain differences of 21 frequencies ranging from 30 kHz to 40 kHz in steps of 0.5 kHz are in each box-and-whisker plot.

## 4.2 Relevance to Bat Biosonar

It was observed that the bat nostrils are “comma-shaped”, which is narrow radially but wide tangentially and can be approximated as elliptical shape. The anterior leaf was attached tangentially. Hence, it can be hypothesized that the comma-shaped bat nostrils create a near-field that is well suited for illuminating the flanges of the anterior leaf and hence create strong effects when the anterior leaf is deformed. It was also found that a bioinspired concave shape creates pronounced

time-variant signatures with just a small displacement (less than  $10^\circ$ ), which could be the function of concave profile of the horseshoe bat anterior leaf. Both those two features enhance the dynamic sensing in bat biosonar.

### 4.3 Relevance to Engineering

In engineering, the shape of horn loudspeaker is convex and it usually operates below 20 kHz. Within this frequency range, the convex horn has higher acoustic resistance compared with the conical and concave horn [111].

While for the shape of the anterior leaf, when compared with other horn provides commonly used in engineering (Fig. 4.4a) using a modal propagation method for numerical estimation of acoustic resistance [105, 106, 107], the concave baffle cross-section of show a resistance maximum just above 80 kHz, which is about 30% higher than other tested horns. This indicates that for engineering device, it is possible to adopt the anterior leaf shape if the device needs to operate in the higher frequency.

Horn loudspeaker and other directivity device, such as antenna, is static in the local sense. For the future design, dynamic features could be added to improve the detection range as the time-variant signature generated by the continuous movement of the concave baffle.

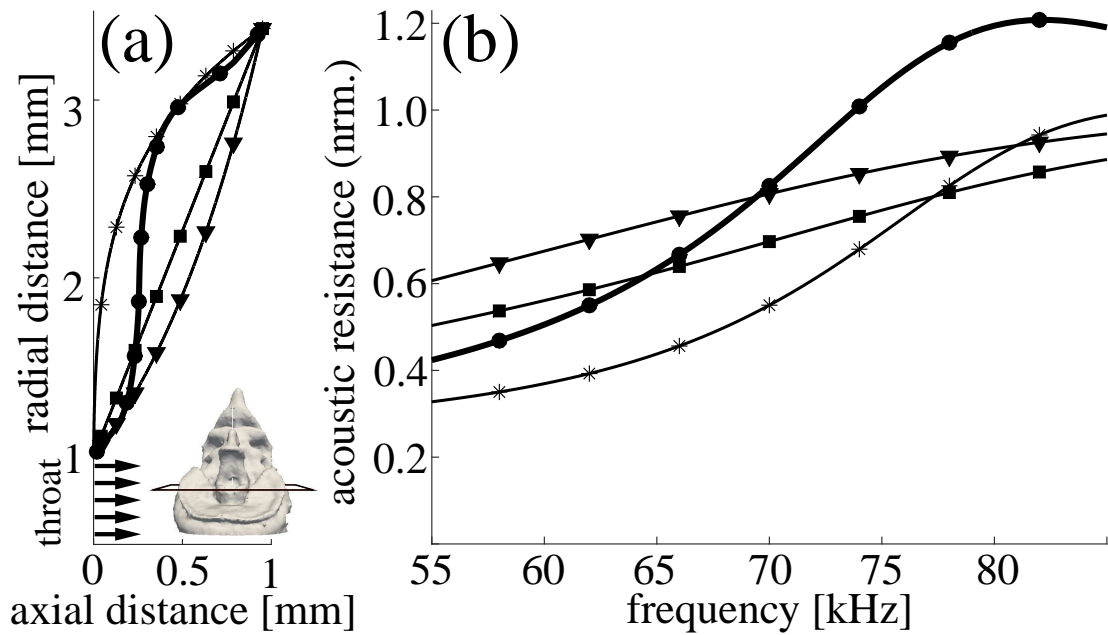


Figure 4.4: A horn approximation of the anterior leaf compared to other horns: a) cross-sections of the anterior leaf (thick line, circles) compared to Bessel (stars), conical (squares), and exponential (triangles) horns, b) numerical predictions of the acoustic resistances (normalized by a plane wave over the throat area of the horns) for the horn cross-sections shown in (a). The inset in (a) shows the cutting plane through the anterior leaf that was used to obtain the anterior leaf cross-section.

# Chapter 5

## Summary

### 5.1 Major Findings

Based on the biological morphology of the bat noseleaf, two prototypes were designed. An automated experimental setup was used to measure the radiation pattern of the two prototypes. Both time domain and frequency domain signal processing methods were used to analyze the experimental data. By doing so, the following major findings were achieved:

1. In the current experimental design, the rotation of the lancet ( $0^{\circ}$ - $5^{\circ}$ ) induced acoustic effects with overall 1 dB beam-gain change.
2. The minor axis direction of the elliptical outlet produces omnidirectional radiation pattern in the far-field.
3. For the straight baffle, the root-mean-square (rms) gain difference between reference angle ( $90^{\circ}$ ) beampattern and tested angle ( $30^{\circ}$ - $80^{\circ}$  in steps of  $10^{\circ}$ ) beampattern linearly depends on the bending angle (reference angle-tested angle).
4. For the concave baffle, the rms gain difference between reference angle ( $90^{\circ}$ ) beampattern and tested angle ( $30^{\circ}$ - $80^{\circ}$  in steps of  $10^{\circ}$ ) beampattern oscillates as bending angle (reference angle-tested angle) increases. But linearly increases as the bending angle increases from  $0^{\circ}$  to  $10^{\circ}$  in steps of  $2^{\circ}$  or  $3^{\circ}$ .
5. To get the same acoustic gain change ( 6dB rms difference), the straight baffle need rotate six times ( $60^{\circ}$ ) more than the concave baffle ( $10^{\circ}$ ).
6. Concave baffle produces a time-variant, frequency-variant signature when rotating it continuously.

## 5.2 Suggestions for Future Work

To gain further insights into bisonar, the following could be done in the future:

1. Systematic experimental and numerical (finite element method) investigate the acoustic properties of convex, conical and concave baffle.
2. Correlate the time-variant signature with the frequency-variant root-mean-square (rms) gain difference.
3. The model developed here is a one dimension model and a more sophisticated model could be created. Individual and interact acoustic effect of the noseleaf model could be investigated.
4. Adding target and echo reception part in the experiment to investigate the engineering aspect of the whole echolocation system.

# Bibliography

- [1] H.T. Arita and M.B. Fenton. Flight and echolocation in the ecology and evolution of bats. *Trends Ecol. Evol.*, 12(2):53–58, Feb. 1997.
- [2] J.R. Speakman. The evolution of flight and echolocation in bats: another leap in the dark. *Mammal Rev.*, 31(2):111–130, Dec. 2001.
- [3] G. Neuweiler. Evolutionary aspects of bat echolocation. *J. Comp. Physiol. A*, 189(4):245–256, Apr. 2003.
- [4] M.B. Fenton. *Just bats*. University of Toronto Press, Buffalo, Toronto, 2nd edition, 1983.
- [5] G. Neuweiler. Foraging, echolocation and audition in bats. *Naturwissenschaften*, 71(9):446–455, Sep. 1984.
- [6] H.U. Schnitzler, C.F. Moss, and A. Denzinger. From spatial orientation to food acquisition in echolocating bats. *Trends Ecol. Evol.*, 18(8):386–394, Aug. 2003.
- [7] C.J. Harper, S.M. Swartz, and E.L. Brainerd. Specialized bat tongue is a hemodynamic nectar mop. *Proc. Natl. Acad. Sci. U.S.A.*, 110(22):8852–8857, May 2013.
- [8] R. Müller and R. Kuc. Biosonar-inspired technology: goals, challenges and insights. *Bioinsp. Biomim.*, 2(4):S146–S161, Oct. 2007.
- [9] D. Russo, G. Jones, and R. Arlettaz. Echolocation and passive listening by foraging mouse-eared bats *Myotis myotis* and *M. blythii*. *J. Exp. Biol.*, 210(1):166–176, 2007.
- [10] J.A. Simmons. The resolution of target range by echolocating bats. *J. Acoust. Soc. Am.*, 54(1):157–173, 1973.
- [11] J.A. Simmons, S.A. Kick, B.D. Lawrence, C. Hale, C. Bard, and B. Escudié. Acuity of horizontal angle discrimination by the echolocating bat, *Eptesicus fuscus*. *J. Comp. Physiol.*, 153(3):321–330, Sep. 1983.
- [12] J.A. Simmons. A view of the world through the bat’s ear: The formation of acoustic images in echolocation. *Cognition*, 33(1-2):155–199, Nov. 1989.

- [13] B. Falk, T. Williams, M. Aytekin, and C.F. Moss. Adaptive behavior for texture discrimination by the free-flying big brown bat, *Eptesicus fuscus*. *J. Comp. Physiol. A*, 197(5):491–503, May 2011.
- [14] M.K. Obrist, M.B. Fenton, J.L. Eger, and P.A. Schlegel. What ears do for bats: a comparative study of pinna sound pressure transformation in Chiroptera. *J. Exp. Biol*, 180(1):119–152, 1993.
- [15] M.E. Bates, J.A. Simmons, and T.V. Zorikov. Bats use echo harmonic structure to distinguish their targets from background clutter. *Science*, 333(6042):627–630, Jul. 2011.
- [16] M.B. Fenton, P.A. Faure, and J.M. Ratcliffe. Evolution of high duty cycle echolocation in bats. *J. Exp. Biol.*, 215(17):2935–2944, 2012.
- [17] EdgeTech. 4200 series side scan sonar system. product brochure, 2014.
- [18] Teledyne Reson. Seabat 7125 - ultra high resolution multibeam echosounder. product brochure, 2014.
- [19] NORBIT. Wideband multibeam sonar. product brochure.
- [20] J.G. Rees. Science, technical innovation and applications in bioacoustics: summary of a workshop. Technical Report CR/04/201, British Geological Survey, Jul. 2004.
- [21] G. Jones and M.W. Holderied. Bat echolocation calls: adaptation and convergent evolution. *Proc. R. Soc. B.*, 274(1612):905–912, Apr. 2007.
- [22] K. Fawcett, D.S. Jacobs, A. Surlykke, and J.M. Ratcliffe. Echolocation in the bat, *Rhinolophus capensis*: the influence of clutter, conspecifics and prey on call design and intensity. *Biol. Open*, 4(6):693–701, Jun. 2015.
- [23] D.R. Griffin and J.A. Simmons. Echolocation of insects by horseshoe bats. *Nature*, 250:731–732, Aug. 1974.
- [24] J.M. Ratcliffe, C.P.H. Elemans, L. Jakobsen, and A. Surlykke. How the bat got its buzz. *Biol. Lett.*, 9(2):20121031, Jan. 2013.
- [25] C.P.H. Elemans, A.F. Mead, L. Jakobsen, and J.M. Ratcliffe. Superfast muscles set maximum call rate in echolocating bats. *Science*, 333(6051):1885–1888, Sep. 2011.
- [26] Y. Shiori, S. Hiryu, Y. Watanabe, H. Riquimaroux, and Y. Watanabe. Pulse-echo interaction in free-flying horseshoe bats, *Rhinolophus ferrumequinum nippon*. *JASA Express Letters*, 126(3):EL80–EL85, Aug. 2009.
- [27] M. Vespe, G. Jones, C. Baker, and D. Blacknell. Biologically inspired waveform diversity for synthetic autonomous navigation sensing. Technical Report RTO-EN-SET-119, University of College London, Nov. 2009.

- [28] E.T. Bick, M.E. Fife, and S.A. Hudson. Bow dome sonar, Jan. 2002. Patent.
- [29] M. Noonan. Design and method for improving the performance of submarine and other water craft sonar sensors, arrays and/or hydrophones, Jul. 2010. Patent.
- [30] J.A. Simmons. Acoustic radiation patterns for the echolocating bats *Chilonycteris rubiginosa* and *Eptesicus fuscus*. *J. Acoust. Soc. Am.*, 46(4B):1054–1056, 1969.
- [31] G.K. Strother and M. Mogus. Acoustical beam patterns for bats: some theoretical considerations. *J. Acoust. Soc. Am.*, 48(6B):1430–1432, 1970.
- [32] H.U. Schnitzler and A.D. Grinnell. Directional sensitivity of echolocation in the horseshoe bat, *Rhinolopus ferrumequinum*. I. Directionality of sound emission. *J. Comp. Physiol.*, 116(1):51–61, Jan. 1977.
- [33] A.D. Grinnell and H.U. Schnitzler. Directional sensitivity of echolocation in the horseshoe bat, *Rhinolopus ferrumequinum*. II. Behavioral directionality of hearing. *J. Comp. Physiol.*, 116(1):63–76, Jan. 1977.
- [34] A. Surlykke, S.B. Pedersen, and L. Jakobsen. Echolocating bats emit a highly directional sonar sound beam in the field. *Proc. R. Soc. B*, 276(1658):835–860, Mar. 2009.
- [35] L. Jakobsen, J.M. Ratcliffe, and A. Surlykke. Convergent acoustic field of view in echolocating bats. *Nature*, 493(7430):93–96, Jan. 2013.
- [36] N. Ulanovsky and C.F. Moss. What the bat’s voice tells the bat’s brain. *Proc. Natl. Acad. Sci. U.S.A.*, 105(25):8491–8498, Jun. 2008.
- [37] C.F. Moss and A. Surlykke. Probing the natural scene by echolocation in bats. *Front. Behav. Neurosci.*, 4:33, Aug. 2010.
- [38] M.S. Lewicki, B.A. Olshausen, A. Surlykke, and C.F. Moss. Scene analysis in the natural environment. *Front. Psychol.*, 5:199, Apr. 2014.
- [39] M. Geva-Sagiv, L. Las, Y. Yovel, and N. Ulanovsky. Spatial cognition in bats and rats: from sensory acquisition to multiscale maps and navigation. *Nat. Rev. Neurosci.*, 16(2):94–108, Jan. 2015.
- [40] G. von der Emde and H.U. Schnitzler. Classification of insects by echolocating greater horseshoe bats. *J. Comp. Physiol. A*, 167(3):423–430, Aug. 1990.
- [41] W.C. Knight, R.G. Pridham, and S.M. Kay. Digital signal processing for sonar. *Proceedings of the IEEE*, 69(11):1451–1506, Nov. 1981.
- [42] S. Stergiopoulos. *Advanced signal processing handbook: theory and implementation for radar, sonar, and medical imaging real time systems*. CRC Press, Boca Raton, FL, 2000.

- [43] B. Vogler and G. Neuweiler. Echolocation in the noctule (*Nyctalus noctula*) and horseshoe bat (*Rhinolophus ferrumequinum*). *J. Comp. Physiol.*, 152(3):421–432, Sep. 1983.
- [44] G. Jones and J.M.V Rayner. Foraging behavior and echolocation of wild horseshoe bats (*Rhinolophus ferrumequinum*) and *R. hipposideros* (Chiroptera, Rhinolophidae). *Behav. Ecol. Sociobiol.*, 25(3):183–191, Sep. 1989.
- [45] N.H. Fletcher and S. Thwaites. Obliquely truncated simple horns: idealized models for vertebrate pinnae. *Acta Acustica united with Acustica*, 65(4):194–204, Mar. 1988.
- [46] N.H. Fletcher. *Acoustic systems in Biology*. Oxford University Press, 1992.
- [47] J. Ma and R. Müller. A method for characterizing the biodiversity in bat pinnae as a basis for engineering analysis. *Bioinspir. Biomim.*, 6(2):026008, May 2011.
- [48] J.E. Hill and J.D. Smith. *Bats: a natural history*. British Museum, London, 1984.
- [49] J.D. Altringham. *Bats: biology and behaviour*. Oxford University Press, Oxford, 1998.
- [50] M. Pannala, S.Z. Meymand, and R. Müller. Interplay of static and dynamic features in biomimetic smart ears. *Bioinspir. Biomim.*, 8(2):026008, 2013.
- [51] J.M. Wotton, T. Haresign, and J.A. Simmons. Spatially dependent acoustic cues generated by the external ear of the big brown bat, *Eptesicus fuscus*. *J. Acoust. Soc. Am.*, 98(3):1423–1445, 1995.
- [52] J.M. Wotton, T. Haresign, M.J. Ferragamo, and J.A. Simmons. Sound source elevation and external ear cues influence the discrimination of spectral notches by the big brown bat, *Eptesicus fuscus*. *J. Acoust. Soc. Am.*, 100(3):1764–1776, 1996.
- [53] T. Shimozawa, N. Suga, P. Hendler, and S. Schuetze. Directional sensitivity of echolocation system in bats producing frequency-modulated signals. *J. Exp. Biol.*, 60(1):53–69, 1974.
- [54] P.H.S. Jen and D. Chen. Directionality of sound pressure transformation at the pinna of echolocating bats. *Hearing Research*, 34(2):101–117, 1988.
- [55] E. Aytekin, M. Grassi, M. Sahota, and C.F. Moss. The bat head-related transfer function reveals binaural cues for sound localization in azimuth and elevation. *J. Acoust. Soc. Am.*, 116:3594–3605, Dec. 2004.
- [56] S. Kim, R. Allen, and D. Rowan. Range dependent characteristics in the head-related transfer functions of a bat-head cast: part 2. Binaural characteristics. *Bioinspir. Biomim.*, 7(4):046015, Dec. 2012.
- [57] B.D. Lawrence and J.A. Simmons. Echolocation in bats: the external ear and perception of the vertical positions of targets. *Science*, 218(4571):481–483, Oct. 1982.

- [58] C. Chiu and C.F. Moss. The role of the external ear in vertical sound localization in the free flying bat, *Eptesicus fuscus*. *J. Acoust. Soc. Am.*, 121(4):2227–2235, Apr. 2007.
- [59] R. Müller. A numerical study of the role of the tragus in the big brown bat. *J. Acoust. Soc. Am.*, 116(6):3701–3712, Dec. 2004.
- [60] R. Müller, H. Lu, and J.R. Buck. Sound-diffracting flap in the ear of a bat generates spatial information. *Phys. Rev. Lett.*, 100(10):108701, Mar. 2008.
- [61] R. Kuc. Model predicts bat pinna ridges focus high frequencies to form narrow sensitivity beams. *J. Acoust. Soc. Am.*, 125(5):3454–3459, May 2009.
- [62] X. Wang and R. Müller. Pinna-rim skin folds narrow the sonar beam in the lesser false vampire bat (*Megaderma spasma*). *J. Acoust. Soc. Am.*, 126(6):3311–3318, Sep. 2009.
- [63] A. Goudy-Trainor and P.W. Freeman. Call parameters and facial features in bats: a surprising failure of form following function. *Acta Chiropterologica*, 4(1):1–16, 2002.
- [64] H.T. Arita. Noseleaf morphology and ecological correlates in Phyllostomid bats. *J. Mammal.*, 71(1):36–47, Feb. 1990.
- [65] H.T. Arita. Description of noseleaves of Phyllostomid bats using Fourier analysis. *Revista Mexicana de Mastozoologia*, 1(1):59–68, 1995.
- [66] C. Dietz. *Aspects of ecomorphology in the five European horseshoe bats (Chiroptera: Rhinolophidae) in the area of sympatry*. PhD thesis, University of Tübingen, Dec. 2007.
- [67] A Monadjem and P.J. Taylor. *Bats of southern and central Africa: a biogeographic and taxonomic synthesis*. Wits University Press, Johannesburg, 2010.
- [68] M.F. Robinson. A relationship between echolocation calls and noseleaf widths in bats of the genera *rhinolophus* and *hipposideros*. *J. Zool. Lond.*, 239(2):389–393, 1996.
- [69] D.J. Hartley and R.A. Suthers. The sound emission pattern and the acoustical role of the noseleaf in the echolocating bat, *Carollia perspicillata*. *J. Acoust. Soc. Am.*, 82(6):1892–1900, Dec. 1987.
- [70] Q. Zhuang and R. Müller. Noseleaf furrows in a horseshoe bat act as resonance cavities shaping the biosonar beam. *Phys. Rev. Lett.*, 97(21):218701, Nov. 2006.
- [71] Q. Zhuang and R. Müller. Numerical study of the effect of the noseleaf on biosonar beam-forming in a horseshoe bat. *Physical Review E*, 76(5):051902, 2007.
- [72] D. Vanderelst, R. Jonas, and P. Herbert. The furrows of Rhinolophidae revisited. *J. R. Soc. Interface*, 9(70):1100–1103, 2012.
- [73] A.K. Gupta, D. Webster, and R. Müller. Interplay of furrows and shape dynamics in the lancet of the horseshoe bat noseleaf. *J. Acoust. Soc. Am.*, 138(5):3188–3194, Nov. 2015.

- [74] Z. Zhang, S.N. Truong, and R. Müller. Acoustic effects accurately predict an extreme case of biological morphology. *Phys. Rev. Lett.*, 103(3):038701, Jul. 2009.
- [75] H. Schneider and F.P. Möhres. Die ohrbewegungen der hufeisenfledermäuse (Chiroptera, Rhinolophidae) und der mechanismus des bildhörens. *Z. Vergl. Physiol.*, 44(1):1–40, Sep. 1960.
- [76] D.R. Griffin, D.C. Dunning, D.A. Cahlander, and F.A. Webster. Correlated orientation sounds and ear movements of horseshoe bats. *Nature*, 196(4860):1185–1186, Dec. 1962.
- [77] J.D. Pye, M. Flinn, and A. Pye. Correlated orientation sounds and ear movements of horseshoe bats. *Nature*, 196(4860):1186–1188, Dec. 1962.
- [78] J.D. Pye and L.H. Roberts. Ear movements in a Hipposiderid bat. *Nature*, 225:285–286, Jan. 1970.
- [79] R.A. Holland and D.A. Waters. Echolocation signals and pinna movement in the fruitbat, *Rousettus aegyptiacus*. *Acta Chiropterologica*, 7(1):83–90, 2005.
- [80] X. Yin, P. Nguyen, T.J. Tucker, and R. Müller. A comparative study of pinna motions in horseshoe bats and Old World leaf-nosed bats. *J. Acoust. Soc. Am.*, 138(3):1761, Sep. 2015.
- [81] J. Mogdans, J. Ostwald, and H.U. Schnitzler. The role of pinna movement for the localization of vertical and horizontal wire obstacles in the greater horseshoe bat, *Rhinolopus ferrumequinum*. *J. Acoust. Soc. Am.*, 84(5):1676–1679, Nov. 1988.
- [82] L. Gao, S. Balakrishnan, W. He, Z. Yan, and R. Müller. Ear deformations give bats a physical mechanism for fast adaptation of ultrasonic beam patterns. *Phys. Rev. Lett.*, 107(21):214301, Nov. 2011.
- [83] R. Müller, M. Pannala, O.P.K. Reddy, and S.Z. Meymand. Design of a dynamic sensor inspired by bat ears. *Smart Mater. Struct.*, 21(9):094025, 2012.
- [84] S.Z. Meymand, M. Pannala, and R. Müller. Characterization of the time-variant behavior of a biomimetic beamforming baffle. *J. Acoust. Soc. Am.*, 133(2):1141–1150, Feb. 2013.
- [85] L. Göbbel. Morphology of the external nose in *Hipposideros diadema* and *Lavia frons* with comments on its diversity and evolution among leaf-nosed Microchiroptera. *Cells Tissues Organs*, 170(1):39–60, 2002.
- [86] W. He, S.C. Pedersen, A.K. Gupta, J.A. Simmons, and R. Müller. Lancet dynamics in greater horseshoe bats, *Rhinolophus ferrumequinum*. *PLoS ONE*, 10(4):e0121700, Apr. 2015.
- [87] L. Feng, L. Gao, H. Lu, and R. Müller. Noseleaf dynamics during pulse emission in horseshoe bats. *PLoS ONE*, 7(5):e34685, May 2012.

- [88] A.K. Gupta, Y. Fu, D. Webster, and R. Müller. Bat noseleaves an an inspiration for smart emission baffle structures. In *Proceedings of the ASME 2013 Conference on Smart Materials, Adaptive Structures & Intelligent Systems*, volume 2, page V002T06A010, Sep. 2013.
- [89] B. Goodman, R. Castro, Y. Fu, R. Müller, and M. Philen. A robotic reproduction of the dynamic sonar sensing in horseshoe bats. In *Proc. SPIE*, volume 9061, page 90614B, Apr. 2014.
- [90] Y. Fu, P. Caspers, and R. Müller. Dynamic baffle shapes for sound emission inspired by horseshoe bats. *J. Acoust. Soc. Am.*, 138(3):1789, Sep. 2015.
- [91] L. Jakobsen and A. Surlykke. Vespertilionid bats control the width of their biosonar sound beam dynamically during prey pursuit. *Proc. Natl. Acad. Sci. U.S.A.*, 107(31):13930–13935, Aug. 2010.
- [92] Y. Yovel, B. Falk, C.F. Moss, and N. Ulanovsky. Active control of acoustic field of view in a biosonar system. *PLoS Biol*, 9(9):e1001150, Sep. 2011.
- [93] N. Matsuta, S. Hiryu, E. Fujioka, Y. Yamada, H. Riquimaroux, and Y. Watanabe. Adaptive beam-width control of echolocation sounds by cf-fm bats, *Rhinolopus ferrumequinum nippon*, during prey-capture flight. *J. Exp. Biol.*, 216(7):1210–1218, Apr. 2013.
- [94] C. Geberl, S. Brinkløv, L. Wiegrebe, and A. Surlykke. Fast sensory-motor reactions in echolocating bats to sudden changes during the final buzz and prey intercept. *Proc. Natl. Acad. Sci. U.S.A.*, 112(13):4122–4127, Mar. 2015.
- [95] P. Kounitsky, J. Rydell, E. Amichai, A. Boonman, O. Eitan, A.J. Weiss, and Y. Yovel. Bats adjust their mouth gape to zoom their biosonar field of view. *Proc. Natl. Acad. Sci. U.S.A.*, 112(21):6724–6729, May 2015.
- [96] L. Jakobsen, M.N. Olsen, and A. Surlykke. Dynamics of the echolocation beam during prey pursuit in aerial hawking bats. *Proc. Natl. Acad. Sci. U.S.A.*, 112(26):8118–8123, Jun. 2015.
- [97] Y.H. Kim. *Sound propagation: an impedance based approach*. Wiley, NJ, 2010.
- [98] M. Pannala. *Design of a biomimetic dynamic microphone baffle*. PhD thesis, Virginia Polytechnic Institute and State University, Dec. 2013.
- [99] Firgelli Technologies Inc. Miniature linear motion series, 112. product brochure.
- [100] Hitec RCD USA Inc. Hs-225bb mighty mini servo, part no: 31225s. product brochure.
- [101] J. W.Thompson. The computation of self- and mutual-radiation impedances for annular and elliptical pistons using bouwkamp’s integral. *J. Sound Vib.*, 17(2):221–233, 1971.
- [102] Y.P. Kathuria. Far-field radiation patterns of elliptical apertures and its annulli. *IEEE Trans. Antennas Propag.*, AP-31(2):360–364, Mar. 1983.

- [103] J.E. Freehafer. The acoustical impedance of an infinite hyperbolic horn. *J. Acoust. Soc. Am*, 11:467–476, Apr. 1940.
- [104] E.R. Geddes. Acoustic waveguide theory. *J. Audio Eng. Soc.*, 37(7-8):554–569, Jul. 1989.
- [105] B. Kolbrek. Simulation of sound propagation in an axisymmetric duct. Technical report, Dec. 2011.
- [106] B. Kolbrek. Modal propagation in acoustic horns, an investigation of the modal propagation method. Technical report, Jun. 2012.
- [107] B. Kolbrek. Modal sound propagation in curved horns of rectangular cross-section. Master's thesis, Norwegian University of Science and Technology, Jun. 2013.
- [108] P.M. Morse. *Vibration and sound*. McGraw-Hill, New York, 2nd edition, 1948.
- [109] H. Suzuki and J. Tichy. Sound radiation from convex and concave domes in an infinite baffle. *J. Acoust. Soc. Am*, 69(1):41–49, Jan. 1981.
- [110] H. Suzuki. *Acoustic radiation and diffraction effects from convex and concave domes*. PhD thesis, Pennsylvania State University, Aug. 1981.
- [111] L.L. Beranek and T. Mellow. *Acoustics: sound fields and transducers*. Academic Press, 2012.